ChemPlusChem

Chemistry Europe
European Chemical Societies Publishing
ChemPlusChem

RESEARCH ARTICLE OPEN ACCESS

From Ink to Mockup: An Integrated Study of Historical Gall Ink Formulations and Their Impact on Paper

Margarida Nunes[1] | Joana Costa Vieira[2] | Ana Paula Costa[2] | Maria Emília Amaral Cabral[2] | Bruno J. C. Vieira[3] | João Carlos Waerenborgh[3] | Helena I. S. Nogueira[4] | Scott G. Mitchell[5] | Ana Claro[6] | Teresa Ferreira[1,7]

[1]Universidade de Évora, HERCULES Laboratory/IN2PAST, Évora, Portugal | [2]FibEnTech-UBI, Fiber Materials and Environmental Technologies, University of Beira Interior, Covilhã, Portugal | [3]C^{2}TN, Centro de Ciências e Tecnologias Nucleares, DECN, Instituto Superior Técnico, University of Lisbon, Bobadela, Portugal | [4]CICECO-Aveiro Institute of Materials, Department of Chemistry, University of Aveiro, Aveiro, Portugal | [5]INMA - Instituto de Nanociencia y Materiales de Aragón, University of Zaragoza, Zaragoza, Spain | [6]CHAM - Centre for the Humanities, College of Social and Human Sciences, NOVA University of Lisbon, Lisboa, Portugal | [7]Universidade de Évora, Escola de Ciências e Tecnologia, Departamento de Química e Bioquímica, Évora, Portugal

Correspondence: Margarida Nunes (Mrmpn@uevora.pt) | Teresa Ferreira (tasf@uevora.pt)

Received: 30 May 2025 | **Revised:** 9 October 2025 | **Accepted:** 2 December 2025

Keywords: artificial ageing | Fe(II) oxalate | iron gall ink | Mössbauer spectroscopy | vibrational spectroscopy

ABSTRACT

Iron gall inks (IGIs) played a central role as a writing medium in Western countries, leaving behind a vast legacy and significant conservation challenges. This study presents a twofold methodological approach to investigate the physicochemical behaviour of IGI-based formulations found in historical Portuguese sources. Fresh and 6-month naturally aged precipitates and supernatant solutions (dried inks) were characterised, and the impact of IGIs on Whatman paper over ageing was studied using attenuated total reflectance Fourier-transform infrared (ATR-FT-IR) spectroscopy, Raman and Mössbauer spectroscopies and X-ray diffraction (XRD). Iron(II) sulphates comprised the primary crystalline phase in the precipitates, while the dried inks consisted of distinct Fe(III)-polyphenol (PPh) complexes. Over time, Fe(III) Mössbauer parameters supported complex structural alterations. IGI-induced degradation on aged mockups was attested by Fe(II) oxalate formation until total depletion of the Fe(III)-PPh fraction. pH, ATR-FT-IR and degree of polymerisation analyses suggested that cellulose oxidation is the primary degradation mechanism, and the physical properties and XRD corroborated that the cellulose structure became disordered over ageing. The ink with the higher weight ratio of Fe(II) sulphate:gallnuts (unbalanced) exhibited the most aggressive action on the support. The results confirm that the more unbalanced the ink composition, the more severe its impact, with ink concentration per surface area also being a critical factor in paper decay.

1 | Introduction

Black inks produced from various materials began as early as the third millennium BC [1, 2]. In the mediaeval period, iron gall ink (IGI) became the preferred medium for writing, mainly due to its indelibility [3, 4]. IGI spans a range of dark colours, from purple–black to grey–brown, depending on its formulation, that is, the components, relative proportions and production methods [2, 3]. Its essential ingredients are green vitriol (a variety of hydrated sulphate richer in iron, also named caparrosa), polyphenol compounds (particularly hydrolysable tannins) of plant origin, such as gallnuts, and a binder like Arabic gum [5, 6]. When Fe(II) sulphate is added to the polyphenol (PPh)-rich extracts, Fe(III) complexes, responsible for the IGI black colour, are obtained. The stronger stabilisation of the Fe(III) over Fe(II) ion by PPh ligands leads to the rapid oxidation of the Fe(II)-pyrogallate complex in the presence of atmospheric oxygen. Binding to polyphenol ligands

lowers the reduction potential of Fe(II), which typically oxidises slowly in the presence of oxygen, accelerating the iron oxidation rate. Over time, water-insoluble, dark pigments precipitate while forming a framework between the organometallic structures [7–9].

The Fe(III)-gallate complex has long been regarded as the primary contributor to IGI colour [9, 10]. However, works on Mössbauer spectroscopy have failed to detect Fe(III)-gallate-based complexes in the analysed inks [11, 12]. This finding is further corroborated by the work of Diaz Hidalgo et al. [13] and Teixeira et al. [7] who, using high-performance liquid chromatography–electrospray ionisation tandem mass spectrometry (HPLC–ESI–MS), reported that the IGI chromophore is primarily composed of iron complexes with pentagalloylglucose and hexagalloylglucose ligands.

Severe decay is often associated with IGI, which endangers worldwide historical written documentation, much of which is already in catastrophic condition. Cellulose degradation is chiefly governed by two mechanisms, that is, acid-catalysed hydrolysis and metal-catalysed oxidation, and IGI is expected to intensify both processes [14, 15]. Hydrolysis of the β-(1,4)-glycosidic bonds, linking the D-glucose units in the cellulose supramolecular structure [15, 16], has been considered by some authors to be the primary mechanism [17, 18]. The contribution of the IGI components to acid hydrolysis, namely gallic acid (GA) and iron solvation complexes, has also been highlighted in several works. During IGI complex formation, the deprotonation of polyphenol molecules occurs upon bonding to the Fe(II) ion, resulting in a pH drop of one unit [9, 16, 19]. Additionally, various acidic additives, such as vinegar (often used in IGI production), may also impact the medium acidity [20].

On the other hand, polyphenol compounds, such as GA, can behave as reducing agents for the Fe(III) ions in the presence of atmospheric oxygen and moisture [21, 22]. Fe(II) ions play a key role in the well-known Fenton reactions, forming reactive radicals that broadly promote cellulose oxidation [15, 23]. Nevertheless, these Fe(II)-driven reactions would increase the pH during ageing since hydroxide ions are produced. It was then argued that only minimal Fe(II) is needed to activate the cellulose oxidation mechanisms. In contrast, Fe(II) oxidation in the presence of oxygen and moisture, similar to the rust-like formation, will induce a pH decrease with the release of hydrogen ions [14, 19]. Moreover, Barański [24] pointed out that oxidising some hydroxyl to carbonyl and/or carboxyl groups in the cellulose backbone weakens the glycoside bonds close to those groups, making them prone to breaking.

Liu et al. [25] attested that IGI does not alter the dominant degradation path experienced by cellulose alone at similar moisture content, suggesting that this parameter may be a key factor for the primary degradation mechanisms. Furthermore, the authors verified that IGI increased the rate of paper degradation by more than 50% compared to uninked papers under the experimental conditions of the study [25]. Hydrolysis plays a critical role in IGI-induced paper degradation; however, when the moisture content is low, oxidation may become a relevant mechanism leading to cellulose chain scission. Briefly, cellulose degradation appears to result from the synergistic action of both mechanisms, with IGI being one of the critical components.

Although IGIs share the same basic ingredients, variations in their formulation and preparation methods might reflect regional, temporal and functional differences. Little is known about the IGIs used in Portuguese documentation, whether civil or religious, or about the specific formulations behind them. To our knowledge, the study by Díaz Hidalgo et al. [13] remains the only detailed research of a Portuguese recipe, considered the oldest known, found in the *Chancelaria de Braga* cx. 31 (1464). Understanding the historical and material context of Portuguese written heritage depends in part on uncovering the specific ink formulations used in its production. Archival research led to the identification of two IGI formulations from the 17th and 18th centuries, hereafter referred to as R_1 and R_2, respectively. Details about the documentation where these formulations were found, as well as their translations after transcription, can be accessed in the Supporting Information (SI) Experimental section.

Neevel [26] noted an official advertisement from the British government in 1889 indicating that 'a stable black IGI should not contain more than three parts of gallnuts to one part of iron (II) sulphate'. According to this author [26], gallnuts contain *ca.* 55 wt% of tannins. Thus, a 'stable black IGI' (later called a balanced ink) should ideally have a molar ratio of 3.6:1.0 (iron sulphate:tannic acid). This reasoning has been widely accepted and replicated in the literature [11, 13, 27]. Both R_1 and R_2 formulations are unbalanced (Table 1), with a surplus of iron sulphate relative to the polyphenol content of the gallnuts (assumed to be tannic acid), although R_2 is notably more unbalanced.

This study adopts an integrated approach, combining multianalytical characterisation with physical testing to examine these ink formulations. The investigation was twofold: i) the analysis of fresh and 6-month naturally aged precipitates, along with the corresponding supernatant ink solutions after drying; ii) the evaluation of ink behaviour on model paper, applied through writing and brushing to simulate historical usage and decoration, and the assessment of their impact on the cellulose support under artificial ageing. We also examined the

TABLE 1 | Summary of the ingredients and quantities to recreate the iron gall inks in the formulations.

Ingredients	R_1	R_2
Gallnuts (g)	86.04	114.72
Tannin content (g)[a]	47.32	63.10
Caparrosa; $FeSO_4{\cdot}7H_2O$ (g)	57.36	114.72
Arabic gum (g)	28.68	86.04
($FeSO_4{\cdot}7H_2O$:tannin:Arabic gum) weight ratio[b]	1.2:1.0:0.6	1.8:1.0:1.4
(Iron sulphate:tannin) molar ratio[c]	7.6:1.0	10.8:1.0
Water (mL)	700	1050
Vinegar (mL)	—	350
Pomegranate peel	1/3 of a fruit peel	—

[a]According to [26], gallnuts contain 55 wt% in tannins.
[b]Weight ratio normalised for the tannin content.
[c]Molar ratio calculated based on the molecular weights of Fe(II) sulphate (278 g mol^{-1}) and tannic acid (1701.19 g mol^{-1}) [11, 26].

degradative effects of IGIs in relation to their degree of chemical imbalance. Lastly, we sought to recreate IGIs based on Portuguese sources, addressing the significant gap in the national literature on this subject.

2 | Experimental

2.1 | Ink Preparation According to the Historical Formulations

Analytical grade $FeSO_4 \cdot 7H_2O$ (99.1%) from Merck (Germany), GA (98.0%) and tannic acid (98.0%) were purchased from Acros Organics (Thermo Fisher Scientific Inc, Massachusetts) and used along with ultrapure water (MiliQ-IQ, Sigma-Aldrich, Germany), to prepare the solutions. Arabic gum in grain form from *Acacia senegal* (L.) Willd. was purchased from Kremer Pigment (Germany), while pomegranate and white vinegar were sourced from a local store. Gallnuts were collected in Idanha-a-Nova from the ground, having fallen from trees of the genus *Quercus*, primarily *Quercus robur* L. and *Quercus pyrenaica* Willd., the dominant species in the region. The fig branch was gathered from a fig tree in Montemor-o-Novo, Portugal. Table 1 details the IGI formulations described in the SI Experimental section.

2.2 | Precipitates and Dried Inks

Freshly prepared IGI solutions (200 mL) for both inks were filtered 1 week after preparation using Büchner funnels (at room temperature (RT) for 30 min) with Whatman filter paper no. 1 under vacuum. The precipitates obtained were lightly rinsed with water, dried at 25°C in an oven for 2 h, transferred to amber-coloured vials (preventing light exposure), and stored at RT (ppt samples). The supernatant solutions were then centrifuged (5 min at 5000 rpm) to remove any remaining solids, placed in Petri dishes and left to dry in an oven (25°C for 48 h). After evaporation, the dried inks (dried supernatant solutions) were collected and stored in amber-coloured vials at RT (*d* samples). The procedure was repeated for IGI solutions at RT, and they were protected from light after 6 months of natural ageing (Table 2).

TABLE 2 | Sample identification and respective ageing period.

	Fresh samples, 1 week	Naturally aged, 6 months
Precipitates	R_1_ppt_1	R_1_ppt_2
	R_2_ppt_1	R_2_ppt_2
Dried inks	R_1_d_1	R_1_d_2
	R_2_d_1	R_2_d_2

2.3 | Mockups and Artificial Ageing Procedure

Isotropic Whatman qualitative filter paper no. 1 (Sigma-Aldrich, USA) with a grammage of 80 g m^{-2} and a thickness of 140 μm was used as the cellulose support for the mockups. This type of paper does not entirely reflect ancient writing paper since it is made of pure cotton and has no sizing. It also has no filler agents [28]. Nevertheless, precisely because of its simplicity, which eliminates the interaction of fillers and sizing and allows the analysis of the cellulose support's behaviour alone, it has been widely used as a paper model in several studies [15, 28, 29].

The historical R_1 and R_2 ink formulations were applied to the cellulose support either by writing with a quill pen or by brushing with a Da Vinci 374 flat brush (size no. 0). These application methods were chosen to simulate traditional writing and painting techniques employed in historical documentation. The ink volume applied per mockup was kept constant and adjusted according to the sheet size. For brushing, a smaller surface area was used to concentrate the ink application (Table SI.8). Sets composed of a variable number of sheet strips in different sizes were prepared according to the chemical characterisation and physical tests to be performed (Table 3). The top part of the sheet strips was intentionally left ink-free to facilitate hanging the mockups on a rack during the ageing tests using pure cotton threads.

TABLE 3 | Whatman mockup strip details: size and volume of the applied ink per strip, application method and the total number of mockups prepared per ink reproduction (R_1 and R_2).

	Mockup strip details		
	Size, w × h, cm^2	Volume of ink per sample, μL	Application method
Analytical characterisation			Brushed/written
Colourimetry, pH, Mössbauer spectroscopy, SEM/EDS, ATR-FT-IR, DP, XRD	6.5 × 2.5	15	10
Physical characterisation			Brushed/written
Dry zero-span	15.0 × 2.5	35	10
Tensile strength and Young modulus	21.5 × 1.5	30	12
Bursting strength	10.0 × 10.0	92	10

The mockups were artificially aged per ink reproduction (R_1 and R_2) in a climatic chamber (Fitoclima 150 EDTU) to prevent in situ contamination. Separately, a third batch of uninked paper was artificially aged to act as a control (reference samples). The procedure was conducted according to ISO 5630–3 [30] (65% RH and 80°C). Ageing periods were defined for 0, 4, 5, 6 and 7 weeks, labelled as t_0, t_1, t_2, t_3 and t_4, respectively. A set comprising ten mockups (five brushed and five written) was removed at each period. The mockups were then left at RT for at least 72 h. Reference samples and mockups were labelled as in Table 4.

3 | Analytical Characterisation

3.1 | Colourimetry

A portable Data Colour Check Plus II colourimeter was utilised for SCE colour measurements under the D65 standard illuminant and a 10° viewing angle. The L*a*b* coordinates within the CIELAB colour space enable the assessment of colour changes over the ageing period. L* expresses the lightness (0 = black, 100 = white). a* and b* are the chromaticity coordinates (green: $a^* < 0$, red: $a^* > 0$; blue: $b^* < 0$, yellow: $b^* > 0$). To quantify the overall colour difference and the changes in individual L*a*b* coordinates following ageing, the values of ΔE^*_{ab} and ΔL^*, Δa^*, Δb^* were calculated. The ΔE^*_{ab} was estimated according to the UNI EN 15 886:2010 protocol [31]. Calibration of the instrument was performed using a white tile and a black trap. To ensure reproducibility, three measurements were taken of both unaged and aged reference samples, as well as in the inked areas of the unaged and aged mockups. The results are presented as the average of these three measurements.

3.2 | pH Measurements

The measurements were carried out using a HI-14 143 flat-tip pH electrode (HANNA Instruments Ltd) coupled to a portable HI-99 171 pH metre. The equipment was automatically calibrated using pH 4.0 and 7.0 buffer solutions before the analysis.

TABLE 4 | Samples identification (id), ageing conditions and ageing period.

Sample id	Ageing conditions	Ageing period
S_t_0	Unaged reference sample	None
$R_1w\_t_0$	Unaged mockups	
$R_1b\_t_0$		
$R_2w\_t_0$		
$R_2b\_t_0$		
S_t_i	Aged reference sample	i = 1, 2, 3 and 4
$R_1w\_t_i$	Aged mockups	
$R_1b\_t_i$		
$R_2w\_t_i$		
$R_2b\_t_i$		

The pH measurements of the fresh extracts from the gallnuts and the inks before their application to paper were performed by immersing the electrode directly into the solutions. The mockups' analysis was conducted by pipetting a drop of ultrapure water (MiliQ-IQ, Sigma-Aldrich) onto the area of interest, and the electrode was placed in contact with the wet surface and held in place until the pH value stabilised (~30–50 s). Five measurements were taken per sample on randomly selected inked areas, and the results were averaged.

3.3 | Mössbauer Spectroscopy

Mössbauer spectra were collected in transmission mode at 295 and 80 K using a conventional constant-acceleration spectrometer and a 25 mCi ^{57}Co source in an Rh matrix. The velocity scale was calibrated using α-Fe foil. Isomer shifts (IS) are given relative to this standard at RT. The absorbers were obtained by separately packing the samples—dried inks, precipitates or mockup fragments—in Perspex holders. Only inked fragments of the brushed mockups were used because they had more ink per surface area, ensuring the accuracy of the measurement. Low-temperature measurements were performed with the sample immersed in a bath cryostat filled with He exchange gas. The spectra were fitted to Lorentzian lines using a non-linear least-squares method [32].

3.4 | Variable-Pressure Scanning Electron Microscopy Coupled With Energy-Dispersive X-Ray Spectroscopy (VP-SEM/EDS)

The mockups were studied using a VP Hitachi S-3700N SEM (Hitachi High-Tech Europe GmbH, Germany) coupled with a Bruker XFlash 5010 SDD EDS spectrometer (Massachusetts). The resolution of the EDS detector is 123 eV at the Mn Kα energy line. The samples were placed on a thin conductive carbon tape and analysed under a pressure of 40 Pa. An accelerating voltage of 20 kV was used for the chemical analyses and imaging in backscattered electron (BSE) mode. Semiquantitative data on elemental composition were obtained using Esprit1.9 software.

3.5 | Fourier-Transform Infrared Spectroscopy With Attenuated Total Reflection (ATR-FT-IR)

Infrared analyses were performed on a Bruker Alpha spectrometer (Bruker Optics and Microanalysis GmbH, Germany) controlled by OPUS 6.5 software and coupled with a single-reflection diamond ATR module. The spectra were obtained in the ATR mode in the 4000–350 cm^{-1} region, with a spectral resolution of 4 cm^{-1} and 128 scans. The background spectrum was collected before the analysis of the samples. Advanced ATR correction was applied using Opus 6.5 software. To facilitate the comparison of spectra, a manipulation command from the Opus 6.5 software based on the Min/Max normalisation method was employed. This method scaled the spectral intensities, setting the minimum absorbance unit at 0 and the maximum at 2. Published data and the IRUG database were used for spectra interpretation.

3.6 | Raman Spectroscopy

The Raman spectra were recorded in a Bruker MultiRAM RFS27 FT-Raman spectrometer. The 1064 nm laser was used at a power of 4 mW, and 2000 scans were recorded for each sample. Spectra interpretation was carried out based on published data.

3.7 | Degree of Polymerisation (DP)

Viscometry determination based on the UNE 57 039-1:1992 standard method was conducted to estimate the average $\overline{DP}$ using a 2 mL glass capillary viscometer (Schott and Gen, Germany) and cupri-ethylenediamine (CED) solvent (Sigma-Aldrich). For each sample, 50 mg was dissolved in 25 mL of water in a 100 mL bottle with a screw cap, which contained five pieces of electrolytic copper. Subsequently, the samples were placed in an automatic shaker for 20 min to facilitate the disintegration of the cellulose fibres. Then, 25 mL of CED solvent was added to each bottle, tightly capped, and the remaining air was expelled manually. The solution was left under mechanical agitation for 120 min. Finally, each solution was added to a viscometer submerged in a constant-temperature bath at 25.0 ± 0.1°C, and the efflux times were estimated. After that, the intrinsic viscosity [η] was calculated, and the DP values were obtained according to the Mark–Houwink–Sakurada equation, $DP^{\alpha} = K \times [\eta]$, where $\alpha = 0.905$ and $K = 0.805$ [33]. The study was conducted only on mockups subjected to the t_2 ageing period (R_1 ink) and the t_1 ageing period (R_2 ink), as well as on respective reference samples.

3.8 | X-Ray Diffraction (XRD)

Powder XRD was used to characterise the dried inks and precipitates. The mockups were analysed in the micro mode (μ-XRD). Analyses were conducted using a Bruker D8 Discover X-ray diffractometer (Billerica, Massachusetts) equipped with a Cu Kα source and a LYNXEYE linear detector. All measurements were performed from 10° to 75° 2θ, with an increment of 0.05° 2θ and a scan speed of 2 s/step. For the μ-XRD analysis, a zero-background sample holder was used. The spectra were interpreted in accordance with the ICDD database (International Centre for Diffraction Data, US) and the literature. The crystallinity index (CrI) was calculated from the μ-XRD patterns using Segal's method (1959) [34] to assess the degree of crystallinity:

$$CrI = \frac{I_{200} - I_{am}}{I_{200}} \times 100 \quad (1)$$

where I_{200} is the maximum intensity of the peak corresponding to the plane with the Miller indices (200) at around 22.7° 2θ, and I_{am} is the intensity of the non-crystalline material (minimum position between the (200) and the (110) peaks) at an angle between 18° and 19° 2θ. The background was subtracted from the diffractograms before CrI evaluation using a baseline correction in constant mode (Origin Pro 8.5 software). The baseline was estimated for the full-region diffractogram (10°–70° 2θ).

The accuracy of Segal's approach has been controversial since it presents drawbacks [35]. As French (2013) [35] has emphasised, in Segal's method, crystallinity measurements in general provide only an approximate indication of the relative proportions of crystalline and amorphous cellulose, without resolving molecular-level details. The Segal CrI is simple to apply using standard diffractometer data and is straightforward to interpret. For these reasons, despite its limitations, Segal's method continues to be used as a first approach to assessing the crystallinity of cellulose.

The crystallite size of cellulose was also deduced using the Scherrer equation [36]:

$$L = \frac{K * \lambda}{\beta * \cos\theta} \quad (2)$$

with L being the apparent crystallite size, K the Scherrer constant with the value 0.94 for spherical grains, λ the wavelength of the radiation used (0.15406 nm for CuKα_1 radiation), β the full width at half maximum (FWHM) in radians, and θ the Bragg angle in radians. The FWHM value was calculated using Origin Pro 8.5 software. This calculation involved curve fitting estimated through Gaussian deconvolution after applying a baseline correction to the 10°–30° 2θ region of each diffractogram.

3.9 | Physical Characterisation

The physical (structural and mechanical) properties of reference samples and mockups were determined before and after the accelerated ageing procedure. Following ISO standards, several tests were conducted to evaluate the impact of the inks on the cellulose support. The tests were performed on the aged mockups after 5 weeks (t_2) for R_1 and 4 weeks (t_1) for R_2 ageing. These specific ageing periods were also selected for the viscometry study due to the physical fragility of the R_2_t_1 mockups at this point. Measurements were performed with the number of replicates specified in Table 3. All samples were stabilised overnight in a conditioned room that met the criteria of the ISO 187:2022 standard (23 ± 1°C and 50 ± 2% RH) prior to testing. Detailed information on all tests, the corresponding ISO standards, and the instruments used is provided in Table 5.

4 | Results and Discussion

4.1 | Inks and Precipitates Characterisation

The initial phase of this work involved a visual assessment and pH measurement of the freshly prepared inks. The ink solutions R_1 and R_2 presented a black colour with a greyish hue, although R_1 appeared lighter than R_2. The deeper colour of R_2 likely resulted from its longer extraction time of 9 days compared to R_1's 2-day extraction. Additionally, using vinegar as a solvent may have enhanced the extraction of polyphenols (PPhs), thereby increasing their availability for ink production [7]. Furthermore, in R_2, the molar ratio of iron sulphate to tannins is 10.8:1.0, compared with 7.6:1.0 in R_1, indicating a higher availability of iron for forming Fe–PPhs complexes, as Sistach & Espadaler [43] observed.

The gallnut extracts for inks R_1 and R_2 exhibited pH values of 3.19 ± 0.08 and 3.03 ± 0.02, respectively. The longer extraction time indicated for R_2, along with the use of a mixed solvent (water and vinegar), likely contributed to the slightly lower

TABLE 5 | Structural and mechanical tests, as per respective ISO standards, and the instruments used.

	Instruments	ISO standard
Structural tests		
Grammage (g m^{-2})	Mettler Toledo PB303 Delta range analytical balance (Mettler Toledo, Ohio, USA).	ISO 536:2019 [37]
Thickness (μm) Apparent density (g m^{-3}) Specific volume (m^3 g^{-1})	Adamel Lhomargy Micrometer MI20 (Adamel Lhomargy, Roissy-en-Brie, France)	ISO 534:2011 [38]
Air permeability Bendtsen method (mL min^{-1})	Andersson & Sorensen Bendtsen Smoothness and Porosity Tester Gurley densometer (Andersson & Sorensen, Copenhagen, Denmark)	ISO 5636:2014 [39]
Mechanical tests		
Dry zero-span (kgf 15 mm^{-1})	Pulmac Z-span 1000 (Pulmac Systems International, Williston, Vermont, USA)	ISO 15 361:2000 [40]
Tensile index (Nm g^{-1}) Young modulus (MPa)	Thwing-Albert Vantage^{NX} universal (West Berlin, NJ, USA),	ISO 1924-2:2008 [40, 41]
Bursting index (kPa m^2 g^{-1})	Messmer Burst tester 1555 PN (DKSH, Zurich, Switzerland)	ISO 2758:2014 [42]

pH of the R_2 extract. Regarding the freshly prepared inks, the obtained pH values of 2.21 ± 0.01 for R_1 and 2.04 ± 0.04 for R_2 agree well with those reported in the literature [7, 44]. The reasoning behind the deprotonation occurring when the Fe(III)-PPh complex forms [9, 13] can explain the decrease in pH in the inks.

4.1.1 | ATR-FT-IR and Raman Spectroscopies

Representative spectra for the fresh and 6-month-aged, dried inks and ppts are presented in Figure 1. Iron sulphate, dried gallnut extracts, and commercial gallic and tannic acids are discussed separately to facilitate the interpretation of the sample spectra (Figure SI.1 and Table SI.3).

According to Falcão e Araújo [45], the bands at 1619, 1423, 1224, and in the range 1080–1038 cm^{-1} in the dried inks spectra (Figure 1a) are generally associated with PPhs compounds. The features at 1713 and 1320 cm^{-1} are distinctive of hydrolysable tannins, while those at 1080, 885 and 754 cm^{-1} indicate gallotannins. Besides, the bands at 1080 cm^{-1} ($\nu_{asym}(SO_4^{2-})$),

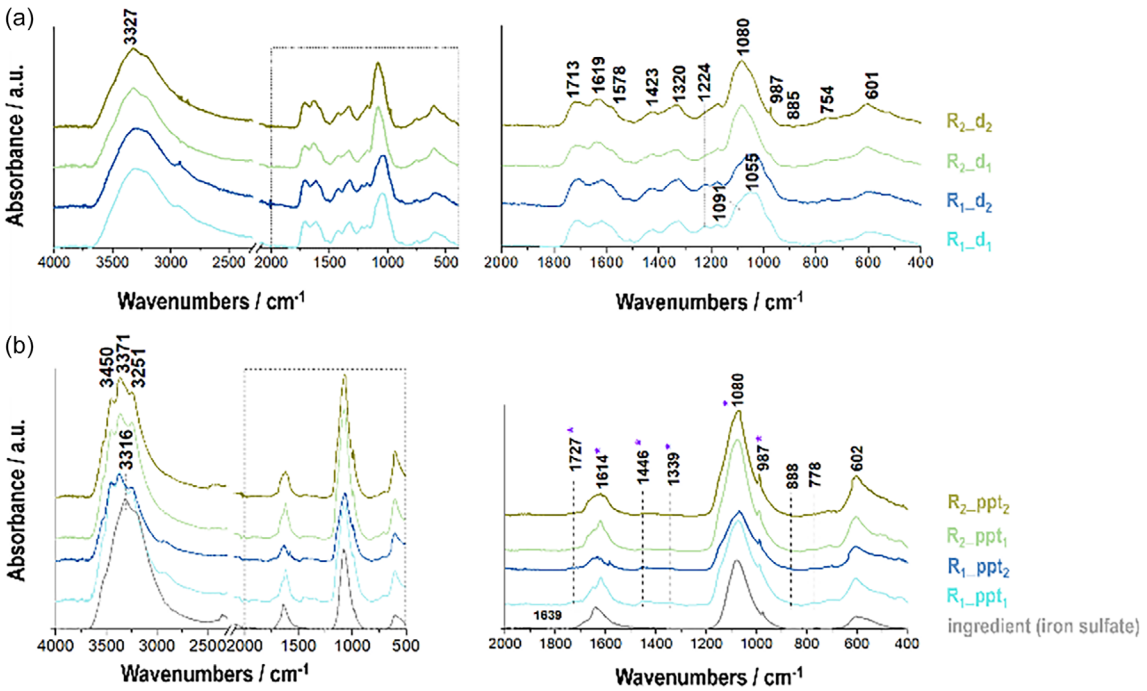

FIGURE 1 | Full region ATR-FT-IR spectra of the (a) dried inks (R_1_d_1, R_1_d_2, R_2_d_1, R_2_d_2) and (b) precipitates (R_1_ppt_1, R_1_ppt_2, R_2_ppt_1, R_2_ppt_2) and ingredient (iron sulphate), along with corresponding insets (2000–400 cm^{-1}). Wavenumbers marked with (*) denote characteristic bands associated with the Fe–PPh complex in the ppts (1727, 1614, 1446, 1339, 1080, 987 cm^{-1}). The spectra are normalised and were vertically offset for clarity. R_1 (recipe of the IGI formulation from Codex 99); R_2 (recipe of the IGI formulation from Memorial of The Secular Canons of St. John the Evangelist Congregation).

987 cm^{-1} ($\nu_{sym}(SO_4^{2-})$) and 601 cm^{-1} ($\delta_{asym}(SO_4^{2-})$) are also characteristic of iron sulphate [46] (Figure 1a, Table SI.4). The complexation of PPhs with iron induces changes in their characteristic vibrational features [46, 47]. For instance, the band at 1031 cm^{-1} (ν_{sym}(C—O)) in the gallnut extract spectra (Figure SI.1) shifts to *ca.* 1055 cm^{-1} (with a smooth shoulder at *ca.* 1091 cm^{-1}) and 1080 cm^{-1} (with a shoulder at 1038 cm^{-1}) in the Fe–PPhs complexes present in R_1 and R_2 inks, respectively. Similar shifts were reported by Espina et al., [47] who attributed them to interactions between iron and –OH groups on the aromatic ring. Another distinctive feature is the reduced intensity of the 1227 cm^{-1} band (ν_{sym}(C—OH)) from the gallnut extract, which appears at 1224 cm^{-1} in R_1 ink and as a subtle shoulder at 1225 cm^{-1} in R_2, providing evidence for the formation of Fe–PPhs complexes [13]. This reduction aligns with observations by Guo et al. [48] in their study of functional metal–phenolic networks. These spectral changes suggest that the development of IGI colour can be associated with iron-catecholate or iron–gallate binding through the phenolic ring, as previously reported [13]. Furthermore, Espina et al. [45] connected a band shift from 731 to 750 cm^{-1} in the Fe–GA spectrum to iron coordination with phenolic –OH groups. A corresponding band at 754 cm^{-1} in R_1 and R_2 spectra supports this interaction. Lastly, a reduction in the intensity of the *ca.* 870 cm^{-1} band, also noted by the authors [47], is mirrored in our data: the band at 888 cm^{-1} in the gallnuts spectrum nearly disappeared in the R_2 and decreases in intensity with a downshift to 885 cm^{-1} in R_1, further indicating Fe–PPh complex formation.

Moreover, the well-defined band at *ca.* 1713 cm^{-1} (ν(C—O)) confirms the presence of a free –COOH group [49]. However, it is well established [50] that upon deprotonation, the carboxylate group typically exhibits two strong bands: one in the 1650–1540 cm^{-1} ($\nu_{asym}(COO^-)$) region and another in the 1450–1360 cm^{-1} region (ν_{sym} (COO^-)). Deacon & Phillips [51] utilised the position and separation between these bands ($\Delta\nu$) to distinguish between different carboxylate coordination modes. Specifically, the separation of 150–200 cm^{-1} can be indicative of chelating and/or bridging coordination modes in metal–acetate complexes. In our spectra, the bands at *ca.* 1578 cm^{-1} ($\nu_{asym}(COO^-)$) and *ca.* 1423 cm^{-1} ($\nu_{sym}(COO^-)$) show a $\Delta\nu$ of 155 cm^{-1}, consistent with iron chelation via the carboxylate group. This suggests that, in addition to the phenolic ring, the IGI complex may also form through interactions involving the COO^- group. A band at *ca.* 601 cm^{-1} (ν(Fe—O)), associated with catechol ring vibrations in Fe–PPhs complexes, was also observed [47, 52], further supporting this coordination. Additionally, bands attributed to iron sulphate are present in the dried ink spectra, with the more intense band at 1080 cm^{-1} in R_2 compared to R_1, corroborating the excess of this ingredient in the R_2 formulation.

The ATR-FT-IR spectra of the ppts (Figure 1b) and their corresponding band assignments (Table SI.5) predominantly display features characteristic of iron sulphate, previously discussed. This indicates that excess reagent precipitated over time. As reported in the literature [53, 54], the spectra closely resemble that of melanterite, particularly the features at 3450, 3371 and 3251 cm^{-1}, which are associated with the –OH stretching vibrations. However, these bands appear more resolved and upward shifted in the ppts spectra compared to the starting material. In addition, minor bands and shoulders attributable to the IGI complex suggested that a minimal amount of Fe–PPh also precipitated from the solution.

Furthermore, the bands observed at *ca.* 1100–1090, 987 and 601 cm^{-1} in the spectra of the dried inks and the ppts may also have contributions from gypsum. This compound is likely formed by the reaction of excess sulphate ions with calcium from the binder, primarily Arabic gum, which is known to contain significant amounts of this element [55]. Additionally, Arabic gum may also contribute to the spectral features at *ca.* 1619, 1423, 1224 and 1090 cm^{-1} in the spectra of the dried inks. This information is detailed in Table SI.4.

The Raman spectra for the R_1 and R_2 ppt exhibited similar characteristics (Figure SI.2, Table SI.6), consistent with features typically assigned to iron–polyphenol complexes found in IGI. No bands corresponding to iron sulphate were detected. The overall signal intensity is low, likely due to the low laser power used during measurements (FT-Raman, 1064 nm laser at 4 mW) to prevent sample degradation. The broadness of the bands suggests a low degree of crystallinity, contrasting with the sharp features reported by Ponce et al. [9] for crystalline Fe(III) gallate. While the major bands of our spectra align with previously published IGI spectra [49, 56], differences in their intensities were observed. The IGI spectra are characterised by two main bands: 1485–1465 cm^{-1} and 1350–1295 cm^{-1} (high to medium intensity) and a shoulder at 640–490 cm^{-1} (medium-to-low intensity) [49, 56]. For iron complexes of GA or pyrogallol (PY), bands have been reported at 1470 (ν_1), 1322 (ν_2) and 576 (ν_3) cm^{-1} for GA–Fe, and 1464 (ν_1), 1299 (ν_2) and 600 (ν_3) cm^{-1} for PY–Fe [47]. The ν_1 band is attributed to the benzene 19*b* vibration (ν(C—C)) coupled with C—O stretching (ν(C—O)) and C—H in-plane scissoring (δ(C—H)) in CH_2 groups, with significant contributions from the stretching of carbon atoms bonded to oxygen. This band, which is weak in free phenol groups, intensifies upon complexation with iron due to changes in polarizability and often dominates IGI Raman spectra [9, 47]. However, in our spectra, it appears slightly less intense than the band observed at 1420 cm^{-1}. The ν_2 band, located between 1345–1295 cm^{-1}, is attributed to C—OH stretching (ν(C—OH)) and in-plane bending modes (δ(C—H), δ(OH)), and is sensitive to the polyphenol structure [47, 49]. The region at 1331–1336 cm^{-1} was found to be the sightliest, most intense in the spectra of Iberian inks and reference compounds prepared by Díaz Hidalgo et al., [57] closely matching our observed band at 1338 cm^{-1}. The ν_3 band reflects the stretching modes of the new Fe—O bonds (ν(Fe—O)), resulting from complexation between the iron cation and oxygen atoms in polyphenolic compounds. The position of the ν(Fe—O) bands can vary depending on the molecular environment [47]. A broad band in the 640–490 cm^{-1} region, also observed by Lee et al. [58] in two 19th-century inked parchment documents, appears in our spectra between 600 and 560 cm^{-1}. Additionally, less intense bands of the Fe–PPhs complexes were observed around 1580, 1430, 1395, 1290, 1217 and 1100 cm^{-1}, with their relative intensities varying depending on the phenolic precursor [47, 56]. Espina et al. [47] reported strong bands for TA and GA at 1711/1613 cm^{-1} and 1692/1615 cm^{-1}, respectively, attributed to the carboxylic acid C—O stretching (ν(C—O)), and the benzene ring 8*a* stretching (ν_{sym}(C—C)) [47, 49]. These bands significantly decrease upon iron complexation, with the higher wavenumber bands nearly disappearing and the lower bands shifting to 1580 cm^{-1} (TA) and 1576 cm^{-1} (GA), consistent with our spectra, particularly the feature at *ca.* 1580 cm^{-1}. Additionally, our spectra display two strong bands [9, 50] at

1580 cm^{-1} ($\nu_{asym}(COO^-)$) and 1420 cm^{-1} (ν_{sym} (COO^-)), with a 160 cm^{-1} separation, indicating the presence of deprotonated carboxylate groups. This supports ATR-FT-IR results and suggests the involvement of carboxylate groups in Fe(III) chelation within the IGI complex.

Collectively, the ATR-FT-IR and Raman results reinforce the roles of both phenolic and carboxylate groups in the formation of the IGI complex.

4.1.2 | XRD

XRD was used to investigate the crystalline fraction in the dried inks and ppts (Figure SI.3). Melanterite was absent in both fresh and 6-month-aged dried inks. The less hydrated phases, rozenite and szomolnokite, were present in both R_1 inks, while szomolnokite was the predominant phase in R_2 dried inks. The drying conditions at 25°C over 2 days likely inhibited the nucleation and growth of the more hydrated iron sulphate phases. Burgaud et al. [59] similarly observed rozenite in the crystalline fraction of dried ink residues from laboratory-prepared IGI, along with a mixture of rozenite and szomolnokite in artificially aged samples. Gypsum was more prevalent in R_2 inks, likely due to a higher weight ratio of Arabic gum relative to tannins and caparrosa in the formulation. In contrast, gypsum was absent in the aged $R_1\_d_2$ sample, likely because it had already precipitated in the corresponding $R_1\_ppt_2$ sample.

Rozenite ($FeSO_4 \cdot 4H_2O$) (PDF ID: 00-019-0632) was the dominant crystalline phase in the fresh ppts ($R_1\_ppt_1$ and $R_2\_ppt_1$) for both inks. After 6 months of natural ageing ($R_1\_ppt_2$ and $R_2\_ppt_2$), melanterite (ideal formula: $Fe(H_2O)_6SO_4 \cdot H_2O$) (PDF ID: 00-22-0633) became the primary phase, though it was already present in the fresh ppts. This phenomenon likely resulted from hydration, with the crystal structure adapting to accommodate more water molecules, thereby increasing the unit cell volume while maintaining the same space group ($P2_1/b$) [60]. In $R_1\_ppt_2$, szomolnokite ($FeSO_4 \cdot H_2O$) (PDF ID: 00-74-1332) was also identified, potentially due to dehydration during drying (25°C, 120 min) and subsequent storage under ambient conditions. The stability fields for melanterite, rozenite and szomolnokite at RT or higher, depending on the RH, are well documented [54, 61, 62]. Gypsum was detected only in the aged ppts, as previously showcased by the ATR-FT-IR data. IGI appears to be entirely amorphous, as no XRD pattern could be attributed to either the IGI-dried ink or the IGI-ppt. Similar results were reported by Ponce et al., [9] who observed that the IGI-ppt and the Fe(III) gallate crystals became amorphous after 1 day to 2 weeks of exposure to air, and even more rapidly during artificial ageing (100°C and high RH).

A summary of the results is presented in Table 6.

4.1.3 | Mössbauer Spectroscopy

Mössbauer spectroscopy is fundamental for assessing the oxidation state and coordination environment of iron and monitoring its changes during chemical transformations. It is worth noting that assigning most of the Fe(III) doublets to specific compounds is challenging or virtually impossible, as similar Mössbauer parameters can be obtained from different compounds with analogous iron environments. Moreover, in some compounds, the iron atoms may be surrounded by different environments, namely in the second or third coordination spheres, resulting in slightly different Mössbauer parameters. Due to the high IS and quadrupole splitting (QS) values and the broader range of these values in the case of high-spin Fe(II) phases, attempts to identify Fe(II) containing compounds are easier than for high-spin Fe(III) compounds. Tentative assignments of the Fe(II) doublets, as well as some trends in the Fe oxidation state, may be deduced from the present Mössbauer study. The spectra of the dried inks (Figures SI.4, SI.5) and the ppts (Figures SI.6 and SI.7) consist of Fe(III) and Fe(II) doublets with distinct parameters (Table SI.7), except for $R_1\_d_1$ and $R_2\_d_1$, which show doublets with similar parameters, although with different relative areas at 80 K. For $R_1\_d_1$ at RT, only a Fe(III) doublet is present (Figure SI.4), while at 80 K (Figure SI.5), a Fe(II) doublet is also observed. The same behaviour was noted for $R_1\_d_2$ and $R_2\_d_1$ inks. The absence of a Fe(II) doublet at 295 K is consistent with the fact that the dried ink samples contained a paste-like phase at this temperature, in addition to a solid phase. Fe(II) in all the dried inks is presumably only present in the paste-like phase, except for $R_2\_d_2$

TABLE 6 | Crystalline phases identified in fresh and naturally aged ppts and dried inks.

Samples	Crystalline phases			
	Melanterite	Rozenite	Szomolnokite	Gypsum
$R_1\_d_1$	—	✓	✓	✓
$R_1\_d_2$	—	✓	✓	—
$R_2\_d_1$	—	—	✓	✓
$R_2\_d_2$	—	—	✓	✓
$R_1\_ppt_1$	✓	✓	—	—
$R_1\_ppt_2$	✓	—	✓	✓
$R_2\_ppt_1$	✓	✓	—	—
$R_2\_ppt_2$	✓	—	—	

ink, where a second Fe(II) contribution from the solid phase was observed at 295 K. This means that the recoilless factor *f* of Fe(II) in the paste-like phase is vanishingly small at 295 K, while at 80 K this phase is frozen, and *f* becomes finite. This paste-like phase was likely due to an excessively short drying period, which was insufficient to completely evaporate the solvent.

On the other hand, the parameters of the Fe(III) doublets in R_1_d_1 and R_2_d_1 are different from those in R_1_d_2 and R_2_d_2 (Table SI.7). This suggests that changes may occur in the Fe(III)-PPh complex over time. While Fe(III) doublets are associated with the solid phase, it is possible that Fe(III)-containing compounds are also present in the paste-like phase. Nevertheless, the parameters are indistinguishable from one another. As summarised in Table SI.7, dried inks are significantly more oxidised than the ppts. This finding aligns with the ATR-FT-IR spectra of the dried inks, which strongly indicate the presence of Fe(III)-PPhs complex, contrary to the ppts' spectra (dominated by iron sulphate). Additionally, XRD results show no evidence of Fe(II)–Fe(III) mixed phases or Fe(III) phases in the dried inks, supporting the conclusion that Fe(III) is solely associated with PPhs in the Fe(III)-PPh complexes.

Regarding the ppts (fresh and aged), the Fe(II) parameters (Table SI.7) may be assigned to rozenite and melanterite, which have similar parameters. In contrast, the more oxidised dried samples, that is, R_1_d_1, R_1_d_2, and R_2_d_1, exhibit Fe(II) parameters that align closely with those of szomolnokite ($FeSO_4 \bullet H_2O$) [11, 22, 63]. This iron phase was identified through XRD analysis in the dried inks. Both the XRD and 80 K Mössbauer studies confirmed the presence of iron sulphate in the dried inks, as inferred from ATR-FT-IR results. Besides, these techniques suggested that all three Fe(II) sulphates are present in R_1_ppt_2 and R_2_d_2. Overall, these findings suggest that during ink preparation, depending on the ratio of the main ingredients, several Fe-containing compounds may form and evolve over time.

Further insights were gained regarding the IGI chromophore complex. The Fe(III) doublets observed in R_1_ppt_1 and R_1_d_2 showed the same parameters as one of the doublets reported by Ponce et al. [9] for the IGI precipitate and crystalline Fe(III) gallate, respectively. These compounds were synthesised using analytical-grade $FeSO_4 \bullet 7H_2O$ and a GA solution, with potassium hydroxide employed to dissolve the GA during the crystal synthesis. The authors attributed the observed doublets to amorphous and crystalline forms of Fe(III) gallates [9]. However, Ponce et al. [9] also identified additional Fe(III) doublets with QS > 1.0 mm s^{-1}, which do not appear in our spectra. Moreover, the remaining doublets observed in our spectra do not match those reported for synthetic crystalline and amorphous Fe gallates in the literature [9, 11, 12]. Interestingly, the estimated Fe(III) parameters for R_2_ppt_1 are, within experimental error, similar to those reported by Gust and Suwalski [64] for a Fe(III)-PPh mono-complex formed from $Fe_2(SO_4)_3 \bullet nH_2O$ and oak tannin (OT). This complex, classified as a CI-type, is suggested to exhibit a catecholate binding mode [64]. According to the authors, the number of phenolic groups on the aromatic ring—provided that there are at least two in *ortho*-positions—and the structure of the residue in the PPh ligand did not seem to affect the IS and QS parameters for the Fe(III)-PPh mono-complex. As a result, the Mössbauer parameters appeared consistent across different ligands. Specifically, the parameters for Fe(III) mono-complexes with catechol, PY, GA and OT do not differ significantly and are better described by a CI-type complex.

In summary, the combined results from ATR-FT-IR, Raman, XRD and Mössbauer spectroscopy suggest that the ppts from both inks contain an amorphous phase, ranging from ~10% to 30%, due to the formation of a Fe(III)-PPh complex network. This is accompanied by a larger crystalline fraction predominantly composed of various hydrated Fe(II) sulphates, primarily rozenite and melanterite. All the sulphate phases are assumed to be part of the crystalline fraction. As Burgaud et al. [57] suggested regarding GA, we also believe there is a competition between PPh compounds and sulphate ions for iron binding. This likely accounts for the prevalence of iron sulphates in the ppts of both inks despite the differing solubility of Fe–PPhs complexes and iron sulphates in aqueous media. Hydrolysable PPh compounds can act as reducing agents in acidic environments, inhibiting Fe(II) oxidation and likely preventing the formation of mixed Fe(II)–Fe(III) phases, as demonstrated by Burgaud et al. [59]. Furthermore, although both inks are unbalanced, the extraction of the PPhs was likely less efficient than anticipated, which explains the low IGI fraction in the precipitates, where iron sulphates dominate (>70%). Conversely, the dried inks are primarily composed of the IGI complex in solution, with 5% < iron sulphate content < 30%. Rozenite and szomolnokite were identified in R_1 dried inks, while the patterns for R_2, both fresh and aged, were dominated by szomolnokite.

Regarding the IGI complex, iron–gallate complexes can be found in both the IGI precipitates and dried inks, though they are more predominant in the latter. Iron binding primarily occurs through the catecholate group, while ATR-FT-IR and Raman analysis further confirm the involvement of the carboxylate group. These findings are consistent with the literature, [6–13] supporting that various Fe–PPhs complexes contribute to the colourant formation.

4.2 | Mockups Characterisation

4.2.1 | Appearance, Colour and pH Study Over Ageing

The inks in the solution appeared black with a greyish hue but turned light grey when applied to paper, showing colour differences between R_1 and R_2 mockups. Photographic images of the brushed and written mockups are shown in Table SI.8. Given that the colour difference (within one std) between the brushed and written mockups for the same ink displayed similar behaviour, we focused our discussion solely on the brushed mockups.

The L*a*b* coordinates for R_1b_t_0 are 77.2 ± 1.1; -0.8 ± 0.1; -1.1 ± 0.1, while for R_2b_t_0, they are 70.5 ± 0.9; 1.2 ± 0.4; 2.5 ± 0.6. R_2b appears darker due to its slightly lower L* values. R_1 has a greater contribution of green and blue (a*, b* < 0), while R_2, with positive a* and b* values, displays a higher presence of red and particularly yellow. Hence, R_1 appears subtly bluish, whereas R_2 is more yellowish.

Artificial ageing resulted in darkening and a shift towards a brownish colour, with R_2 retaining a slightly more yellow hue. The underlying causes of these colour changes are not yet completely understood. Based on a chromatographic study, Ferretti et al. [29] identified intermediates or side-products arising from the oxidation of GA to ellagic acid, as well as from the subsequent degradation of

ellagic acid-catalysed by Fe(III). The authors [29] attributed these reactions to the darkening observed in IGI.

To evaluate the impact of artificial ageing on colour, we compared the aged mockups (for each ageing period) and the reference (S) samples to the unaged samples, expressing the result as global colour variation (ΔE^*_{ab}) (Figure SI. 8a, b, Table SI. 9 and subsequent discussion). The ΔE^*_{ab} values consistently exceeded the perceptibility threshold ($\Delta E^*_{ab} = 3.0$), indicating noticeable changes to the naked eye.

Whatman paper presents an almost neutral surface pH (6.55 ± 0.31 for the S samples). When the inks were brushed, the pH values decreased by ~42% for the R_1 mockups and ~58% for R_2 (Figure SI.8c and Table SI.10) due to the acidity of the inks. During artificial ageing, a slight decline in pH was observed in both the reference samples and the mockups. Notably, the R_1 ink exhibited a more pronounced drop in pH. Similarly, Ciglanská et al. [65] reported an immediate pH drop following the application of IGI on parchment samples, with further decreases noted during artificial ageing.

4.2.2 | Iron Oxidation State and Coordination Environment Over Ageing

Fe^{57} Mössbauer measurements were carried out on the three sets of samples: S_t_0 (reference samples), unaged (R_1b_t_0 and R_2b_t_0) and aged (t_1 and t_2) mockups. The estimated parameters are presented in Table SI.11, and the spectra in Figures SI.9 and SI.10. No Fe was detected in the reference sample spectrum collected over several days, confirming that the observed doublets in the mockups resulted from the ink or the potential products caused by its interaction with the cellulose support. The notable differences between the unaged mockups and the dried inks suggest that the compounds in IGI are highly unstable and promptly react upon contact with the cellulose support during ageing.

Both R_1b_t_0 and R_2b_t_0 appear more oxidised, with complete oxidation observed in R_1b_t_0. In R_2b_t_0, a small amount of Fe(II) was identified as szomolnokite (Table SI.11). Interestingly, the IS and QS values for Fe(III) in these mockups are similar, within the experimental error, to those reported by Gust and Suwalski [64] for the CI-type Fe(III)-PPh mono-complex prepared with GA and OTs, featuring catecholate binding (Mössbauer spectroscopy in Inks and Precipitates Characterisation section). For the aged mockups, the Fe(III) doublets (Table SI.11) do not match those of synthetic crystalline or amorphous Fe gallates reported in the literature [9, 11, 12]. After the first ageing period (t_1), both R_1b_t_1 and R_2b_t_1 showed a substantial reduction in the Fe(III) ions. In R_1b_t_1, ~60% of the Fe appears as Fe(II) oxalate, while the remaining Fe(III) doublet exhibits different parameters from those found in unaged R_1b_t_0 (except for the IS) and R_2b_t_0 mockups. After 5 weeks of ageing (t_2), all the Fe in the R_1b_t_2 mockups was found to be present as Fe(II) oxalate. In the R_2 mockups, Fe(III) was reduced entirely during the t_1 ageing period, with Fe(II) primarily attributed to Fe(II) oxalate and a minor fraction originating from szomolnokite. Notably, Fe(II) has also been detected in both historical IGI samples [66–68] and modern model samples [11], ranging from *ca.* 15% to 52% of the total Fe content [69]. As ageing progresses, the Fe(II) oxalate fraction increases while szomolnokite decreases in R_2b samples. The presence of oxalates in these samples is significant, as oxalic acid is a byproduct of the oxidative degradation of many organic compounds [70]. In the context of IGI on paper, oxalic acid may result from the degradation of the binder (typically Arabic gum), PPh compounds and cellulose support materials [67, 67, 71–74] or from a combination of these factors. The oxalate ion can then compete with sulphate for Fe(II), leading to the formation of Fe(II) oxalate.

4.2.3 | Morphological Features

The unaged mockups, both brushed and written, displayed an atypically smooth and barely visible ink layer, contrasting with the characteristic textured appearance of historical IGIs [17, 27]. This morphological aspect is attributed to the use of Whatman paper, a thin, unsized cotton paper without fillers, that readily absorbs the ink into its fibres. Upon artificial ageing, the mockups showed a substantial accumulation of dispersed particles on the fibre surface (Figure 2). These particles appeared as agglomerates of micro-sized prismatic, needle-like or rod-shaped crystals.

The ageing process involved exposure to a hot, humid and aerated environment over several weeks, promoting crystal formation in the inked areas. Fe was detected in these crystal agglomerates, either alone or associated with S (Figure 2). However, EDS alone cannot determine their precise composition. As shown by Mössbauer spectroscopy, oxalates formed during artificial ageing and became predominant in both mockups after 4 weeks (Table SI.11). Notably, Fe(II) oxalate was absent in the unaged mockups, as well as in the fresh or aged inks and precipitates, indicating that its formation is linked with IGI degradation.

4.2.4 | ATR-FT-IR and DP

ATR-FT-IR played a crucial role in characterising the mockups at a molecular level and in monitoring ageing-related changes in the cellulose support fostered by the presence of IGI. All spectra (Figures 3 and SI.11) showed the typical features of cellulose I [75–79], with

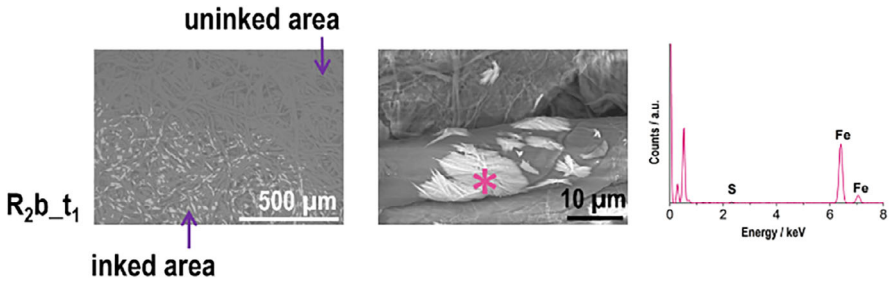

FIGURE 2 | R_2b_t_1 mockup showing dispersed Fe-rich crystals on the inked area (left); a close-up micrograph of the crystals (centre); and corresponding EDS spectrum (right).

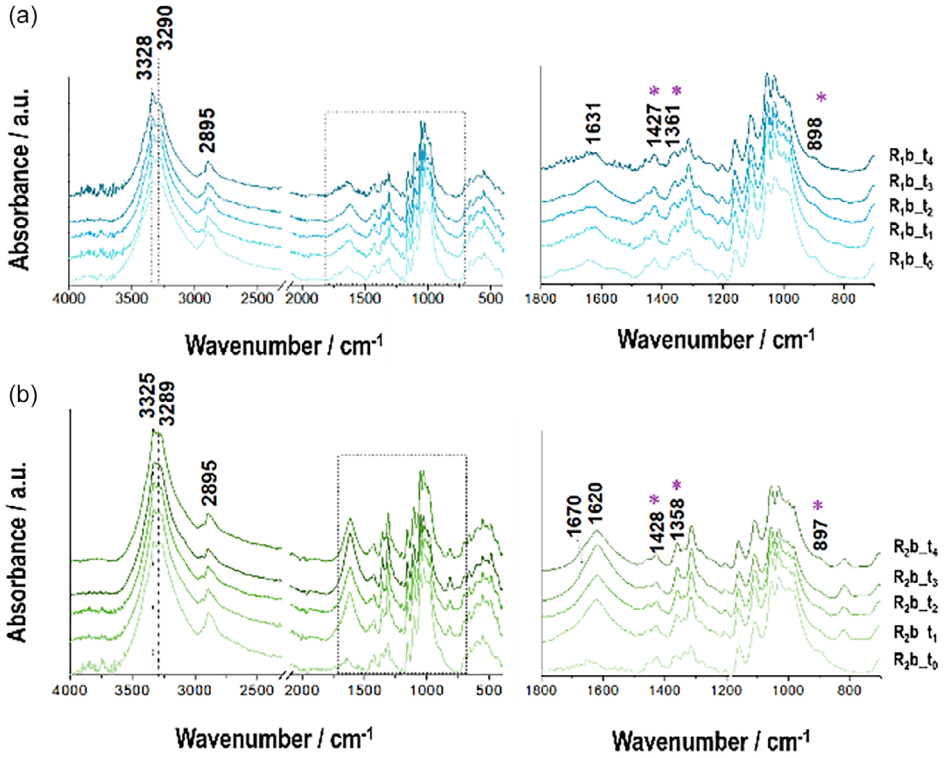

FIGURE 3 | (a,b) FT-IR full-region spectra for the unaged (t_0) and aged (t_1–t_4) R_1b and R_2b mockups, respectively, with insets focusing on the region of interest (1800–700 cm^{-1}) and highlighting major spectral differences associated with structural changes in the cellulose support. A purple asterisk indicates key bands associated with cellulose crystallinity. The spectra are normalised and vertically offset for clarity, with colour grading to enhance visualisation. R_1b (mockup with ink from recipe 1 applied to the cellulose support by brushing); R_2b (mockup with ink from recipe 2 applied to the cellulose support by brushing).

characteristic bands at *ca.* 3328 and 3290 cm^{-1} (ν_{sym}(OH) of intra- and intermolecular H-bonding), 2895 cm^{-1} (ν(CH_2)), 1631 cm^{-1} (δ(OH) of adsorbed water), 1427 cm^{-1} (δ(CH_2)) in crystalline cellulose I), 1361 cm^{-1} (δ(CH)) in crystalline cellulose I), 1318 cm^{-1} (δ(CH_2)), 1161 cm^{-1} (ν_{asym}(C—O—C)) of the β-(1-4)-glycosidic bond), 1107 cm^{-1} (ν_{sym}(C—O)) at C_3 of the glucopyranose ring) and 898 cm^{-1} shoulder in cellulose I (ν_{sym}(C—O—C) at β-(1-4)-glycosidic bond). Furthermore, seven IGI-specific bands at *ca.* 1652–1620, 1448, 1426, 1320, 1106, 1031 and 987 cm^{-1} (previously identified in the Inks and Precipitates Characterisation section and Tables SI.4 and SI.5) were also observed in the mockups' spectra.

Ageing induced clear spectral changes in the mockups compared to the unaged and reference samples. Only the most significant alterations in band shape or position are discussed here. The band at 3328 (ν_{sym}(OH)) (Figure 3a) became slightly narrowed and downshifted, while the band at 3290 cm^{-1} (ν_{sym}(OH)) showed a marked decrease in intensity, particularly in the R_1 mockup.

Alterations in the OH– features can be associated with the cleavage of intra- and intermolecular H-bonds, indicating structural changes in the cellulose support. This observation is consistent with previous studies, irrespective of the model paper [77, 79]. Additionally, a slight drop in intensity and an upward shift of the 2895 cm^{-1} (ν(CH_2)) band further support an increase in amorphous cellulose content in the aged mockups [77]. In the carbonyl region, bands at 1631 cm^{-1} (R_1) and 1620 cm^{-1} (R_2) were observed. Although commonly attributed to δ(OH) of bound water, these bands may also reflect early oxidation products, as suggested by Łojewska et al. [80]. The authors conducted an in situ ATR-FT-IR study in which the bound water was desorbed from paper to evaluate the features in the carbonyl region alone. Based on this, the authors proposed a sequential oxidation mechanism for the C—OH groups in the glucopyranose rings, producing a variety of compounds where the carbonyl groups (band *ca.* 1620 cm^{-1}) corresponded to partial oxidation and the carboxyl or aldehyde groups (band *ca.* 1730 cm^{-1}) indicated the final oxidation stage. Additionally, Henniges et al. [81] highlighted that the interpretation of carbonyl formation in cellulose is complex: hydrolytic cleavage (chain scission) generates reducing ends, while oxidation introduces carbonyls along the chain without necessarily causing chain scission. These two processes are thus intimately linked but mechanistically distinct.

In our samples, although the bands at *ca.* 1631 cm^{-1} (R_1 mockups) and 1620 cm^{-1} (R_2 mockups) were influenced by bound water due to the 65% RH during ageing, comparison with the S samples spectra (Figure SI.11) revealed an increase in band intensity, particularly in the R_2 mockups. Hence, this behaviour is consistent with the C—OH oxidation to carbonyl groups, as observed by Łojewska et al., [80] suggesting that IGI intensifies oxidation relative to traditional paper ageing.

The bands at 1427, 1361 and 898 cm^{-1} are commonly associated with cellulose I, and changes in their shape and intensity are often used to study variations in the degree of crystallinity [46, 82, 83]. Tribulová et al., [84] in their examination of cellulosic materials treated with different metal salts (e.g., Fe(II), Cu(II)) and subjected to artificial ageing, reported that the

broadening of these bands indicated a more disordered structure. During artificial ageing, the 1427 and 898 cm^{-1} bands in the mockups showed greater broadening than in the S samples, suggesting a reduction in cellulose crystallinity [76]. This decrease can be attributed to the presence of IGI.

To further explore the impact of IGI, we estimated the DP of the mockups before and after accelerated ageing using the viscosity method [15, 25]. The results were then compared to those obtained for the Whatman paper (Figure SI. 12). In the literature [15, 19, 85, 86], the DP is often estimated from intrinsic viscosity using the Mark–Houwink–Sakurada equation (Experimental section). However, variations in DP values may occur due to differences in the coefficients (α and K) employed, as reported in prior studies [86–88]. Furthermore, it is known that when used directly on oxidised cellulose, it may underestimate absolute DP values. Therefore, the focus here is placed on the trends observed between samples [80]. Despite these potential discrepancies, our DP values and their ageing trends over time aligned well with the findings of Zaccaron [15], who studied Whatman paper containing IGI under artificial ageing conditions.

Our S samples exhibited decreasing DP values, with a more substantial drop observed after the 4-week ageing period (S_t_1) (Figure SI.12). In contrast, a much smaller decreasing trend was noted after 5 weeks of ageing for S_t_2. Similarly, the mockups displayed an overall declining trend in DP during the ageing process, irrespective of the ink used. This trend intensified in the brushed mockups $R_1b\_t_2$ and $R_2b\_t_1$ compared to their written counterparts $R_1w\_t_2$ and $R_2w\_t_1$.

The pronounced impact of the brushed mockups highlights the influence of concentrated ink. This behaviour aligns with the findings of Rouchon et al. [19] who established that oxygen is the primary driver of cellulose depolymerisation, especially in iron-containing samples within an acidic medium, where chain scissions are mainly ascribed to oxidative mechanisms. The authors [19] also noted that iron, especially Fe(II), catalyses degradation via Fenton-like reactions, even in very low oxygen conditions, and highlighted that depolymerisation occurs faster in concentrated samples, primarily due to the higher Fe(II) content. Similar conclusions were drawn by Zaccaron [15]. Although only minimal Fe(II) is required to initiate Fenton-like reactions, the surplus of Fe(II) in concentrated inks increases the likelihood of these reactions [19]. Oxidation appears to be the primary process responsible for degrading our mockups, particularly the R_2 mockups. Although R_2 ink on paper is slightly more acidic than R_1, the acidity of both inks tends to level over time (Figure SI. 8c), suggesting that acid hydrolysis is unlikely to be the main cause of the fragility already observed in the R_2 mockups after 4 weeks of ageing.

In short, the DP results corroborate the trends observed in ATR-FT-IR data, reinforcing the idea that oxidative mechanisms play a critical role in cellulose degradation in our mockups. The impact of the R_2 ink is notably more severe than that of R_1, with the brushed mockups showing the most considerable degradation.

4.2.5 | XRD

Whatman paper presents a high degree of crystallinity, which can experience significant alterations due to ink interaction [89]. XRD analysis was performed on the mockups to investigate the structural changes during ageing. Native cellulose (cellulose I) exists in two polymorphs, Iα and Iβ, with chains organised in sheets packed in a parallel configuration, which structurally differ [36, 90]. Figure SI.13 shows the XRD patterns for the unaged and aged S samples, as well as the mockups, including the corresponding Miller indices. All samples are confirmed as Iβ-type cellulose, based on the diffraction peaks at *ca.* 14.7°, 16.8°, 22.7° and 34.5° 2θ, corresponding to the Miller indices $(1\bar{1}0)$, (110), (200) and (004), respectively [36, 90]. Under our analytical conditions, the peaks (012) at 20.3° 2θ and (102) at 20.6° 2θ, which typically appear as shoulders on the (200) peak, were absent. This absence allowed a straightforward estimation of the Segal amorphous intensity at 18.2° 2θ [34, 91].

A decrease in the intensity of the (200) peak and a broadening of the $(1\bar{1}0)$ and (110) peaks indicate a crystalline-to-amorphous phase transformation during ageing [89]. This change was subtle in the support material alone (S samples), becoming more pronounced only in the S_t_4 sample. In contrast, the mockups exhibited significant changes much earlier: noticeable broadening of the $(1\bar{1}0)$ and (110) peaks start at the t_1 period, and the ratio of their intensities continued to increase throughout the ageing process (Figure SI.13b, c). The (200) peak, which was initially more intense after the 4-week ageing period, gradually sharpened and decreased with prolonged ageing.

The CrI was estimated using Segal's method [34]. For the S_t_0 sample (Table 7), this parameter exhibited a value of 87%, which is in good agreement with previously reported values for Whatman paper [34, 92]. This value decreased in the S_t_4 sample, indicating the impact of artificial ageing on the support. The unaged S sample seemed to present higher crystallinity than the unaged mockups $R_1b\_t_0$ and $R_2b\_t_0$, suggesting that the ink itself may have interfered with the cellulose structure. This finding is consistent with both the ATR-FT-IR and the

TABLE 7 | The crystallinity index (CrI (%)) and the apparent crystallite size (L (nm)) for the (200) peak.

Sample id	CrI (%)	$L_{(200)}$
S_t_0	87	5.27
S_t_1	87	5.16
S_t_2	86	5.28
S_t_3	86	5.32
S_t_4	79	5.32
$R_1b\_t_0$	78	5.63
$R_1b\_t_1$	78	5.94
$R_1b\_t_2$	77	6.04
$R_1b\_t_3$	78	6.06
$R_1b\_t_4$	57	6.26
$R_2b\_t_0$	70	5.84
$R_2b\_t_1$	77	5.90
$R_2b\_t_2$	79	6.07
$R_2b\_t_3$	79	6.19
$R_2b\_t_4$	67	6.39

DP results. Additionally, the increased background in the diffractogram further indicated the lower crystallinity of the mockups.

During artificial ageing, the CrI of R_1b tend to remain stable until the t_3 period. In contrast, $R_2b\_t_2$ showed an increasing trend in CrI, a phenomenon previously linked to a selective breakdown of less stable amorphous regions in the cellulose matrix during initial ageing stages [92–94]. Besides, Chen et al. [95] reported that transition metal salts selectively degrade the amorphous regions of cellulose, thereby enhancing the CrI. In the later stage of ageing (t_4), the CrI of both R_1b and R_2b mockups present a dropping trend. This reduction has also been reported in the literature [84, 92, 94], suggesting that the crystalline regions are now undergoing degradation. This trend is consistent with the broadening of 1427 cm^{-1} and 898 cm^{-1} bands observed in the ATR-FT-IR spectra during ageing, indicating a shift towards a less ordered structure.

An increase in both the $L_{(200)}$ and CrI values is typically associated with a reduction in the amorphous regions [96, 97]. However, our results showed an opposite trend: although $L_{(200)}$ values generally increased in the mockups, the CrI decreased. A similar trend was observed in the S samples. This behaviour in the crystallite size may be attributed to the sharpening of the diffraction peak at 22.7° 2θ during ageing. A tentative explanation, based on the work of Driemeier et al. [98] on the structural evolution of cellulose crystals from sugarcane subjected to various treatments, suggests that such peak sharpening could result from the aggregation of some laterally joined microfibrils, leading to aggregated crystallites larger than the original individual microfibrils. Additionally, recrystallisation may occur in specific regions where 'nuclei' for crystallite growth form during annealing at a constant temperature, contributing to an overall increase in average crystallite size [99].

Young's modulus of fibres reflects the cellulose chain organisation, that is, highly oriented fibres have higher values, while those with medium-to-low orientation show reduced moduli [94, 100]. The IGI impact on the support became evident through the significant decrease in this modulus over time (Figure SI.14). The brushed mockups presented the smallest drop, with reductions of 77% and 78% for $R_2b\_t_1$ and $R_1b\_t_2$, respectively, compared to their unaged counterparts. Cocca et al. [94] observed a similar trend in their testing of Whatman samples subjected to chemical oxidation treatments, which only partially replicates the IGI-induced degradation. Interestingly, the written mockups showed a less pronounced difference, highlighting the impact of higher ink concentration per surface area on the degradation process. Regarding the S samples, a decrease in Young's modulus was observed from the t_0 to t_1 ageing period, followed by an increase during the t_2 ageing period. This trend has been similarly reported in the literature [94, 101] for cellulose samples subjected to artificial ageing in a climatic chamber.

4.2.6 | Physical Properties

The structural characterisation of the unaged and aged S samples (S_t_0–t_2) and mockups ($R_1b\_t_0$, $R_1b\_t_2$, and $R_2b\_t_0$, $R_2b\_t_2$) involved measuring key parameters such as grammage, thickness, apparent density and the air permeability using the Bendtsen method (Table 2 and Table SI.12). Here, we focus on the mechanical properties which were evaluated through various tests, including tensile strength, bursting strength and dry zero-span (Figure 4).

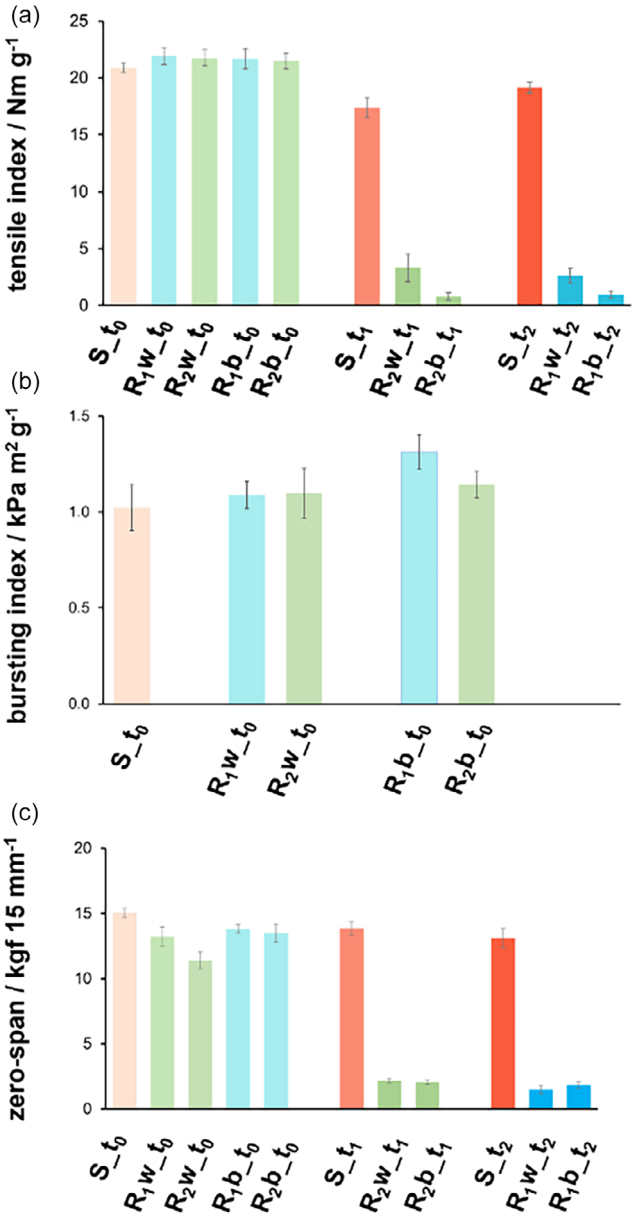

FIGURE 4 | Variation in physical properties of the cellulose support when IGI is used and artificially aged: (a) tensile index (N m g^{-1}); (b) bursting index (kPa m^2 g^{-1}); (c) zero-span (kgf 15 mm^{-1}). Colour grading is used for better visualisation.

The tensile strength test measures the maximum stress a material can withstand before breaking (ISO 1924-2:2008 [41]), while the bursting strength test assesses the material's resistance to rupture under applied pressure (ISO 2758:2014 [42]). Unfortunately, the fragile condition of the aged mockups compromised the reliability of the bursting strength measurements, so this test was only conducted on unaged mockups. The dry zero-span test evaluates fibre damage, considering factors such as fibre cell wall thickness and fibre diameter [102]. No considerable differences were found between the unaged and aged S samples across the various tests (Figure 4). In contrast, the tensile strength of the mockups decreased markedly with ageing, dropping by 70% for $R_1w\_t_2$ and 90% for $R_1b\_t_2$ (Figure 4a). Analogous trends were obtained for the R_2 mockups, in agreement with findings reported by

Feber et al. [103]. It is worth noting that the unaged mockups (t_0) exhibited no substantial variation compared to the unaged S samples, indicating that the ageing process amplified the IGI's impact. Moreover, the dry zero-span test (Figure 4c) showed a pattern similar to that of tensile strength in the aged mockups, suggesting that the the presence of ink compromised the fibres integrity.

Briefly, the physical tests evidenced the detrimental effect of IGI on the physical properties of the paper support. Although both R_1 and R_2 mockups showed comparable decreases in the physical performance, the R_1_t_2 sample underwent an additional week of ageing relative to R_2_t_1, highlighting the more aggressive nature of the R_2 ink formulation.

5 | Conclusions

In this study, we present a comprehensive, multi-analytical investigation of IGI reproductions, examining both precipitates and dry inks, their evolution during ageing, and the impact of the inks when applied to cellulose supports (mockups). Both IGI formulations include an excess of Fe(II) sulphate relative to gallnut content (ingredients), with R_2 showing the greater imbalance. The precipitates primarily consisted of a crystalline fraction of various hydrated Fe(II) sulphates (rozenite and melanterite) along with a minor fraction of amorphous Fe(III)-PPh complexes. Natural ageing has led to a decrease in the fraction of amorphous Fe–PPhs complexes and an increase in Fe(II) sulphates. The presence of these hydrated Fe(II) sulphate phases mirrors the ability of the PPh compounds to act as reducing agents, thereby limiting iron oxidation. Conversely, in the dried inks, Fe(III) in the IGI complex consistently emerged as the dominant phase. Vibrational spectroscopy indicated that the catechol ring or carboxylic acid group (gallate) from the PPhs was involved in complex formation. Mössbauer spectroscopy supported these findings, providing estimated parameters for the Fe(III)-gallate and the Fe(III)-PPh mono-complexes with binding occurring through the catecholate group. Furthermore, differences in the Fe(III) doublets between fresh and 6-month-aged dried inks suggested that the IGI complex structure underwent changes during ageing.

In the mockups, Mössbauer spectroscopy revealed a progressive reduction of Fe(III) and the formation of Fe(II) oxalate over time, with complete depletion of Fe(III) occurring after 4 to 5 weeks of ageing, depending on the ink formulation. Fe(II) oxalate formation has been linked to the IGI's role in promoting the degradation of cellulose support. The combined spectroscopic study provided new insights into the IGI complex within the mockups. The Mössbauer parameters were consistent with Fe(III)-PPh mono-complexes involving catecholate binding. However, during artificial ageing, the parameters shifted and did not match any Fe(III)-PPh complexes described in the literature, indicating that these compounds readily evolve under conditions of relatively high temperature and humidity (65% RH and 80°C), with Fe(III) reduction being favoured in contact with cellulose support.

ATR-FT-IR analysis suggested partial oxidation of C—OH groups in the glucopyranose ring to carbonyl groups, highlighting the crucial role of oxidation mechanisms promoted by the Fe(II) ion in the observed cellulose degradation within the mockups. Mechanical testing demonstrated that ageing, amplified by IGI, negatively impacted the orientation and strength of the cellulose fibres. The brushed mockups, which had a higher concentration of ink per surface area, showed a more pronounced decline in physical properties. Additionally, the more unbalanced ink had a greater detrimental effect on the cellulose support and its properties.

Overall, this study employed a comprehensive approach to thoroughly investigate IGIs, their behaviour over time, and their impact on the support, departing from traditional methodologies. In parallel, this investigation enabled the reconstruction of IGI formulations documented in Portuguese sources, which have remained underdiscussed in the literature.

Author Contributions

Margarida Nunes: conceptualization (lead), data curation (lead), formal analysis (lead), investigation (lead), methodology (lead), validation (lead), visualization (lead), writing – original draft (lead), writing – review and editing (lead). **Joana Costa Vieira**: data curation (equal), formal analysis (lead), methodology (equal), writing – review and editing (supporting). **Ana Paula Costa**: data curation (equal), formal analysis (equal), methodology (equal), writing – review and editing (supporting). **Maria Emília Amaral Cabral**: data curation (equal), formal analysis (equal), methodology (equal), writing – review and editing (equal). **Bruno J. C. Vieira**: data curation (equal), formal analysis (equal), writing – review and editing (equal). **João Carlos Waerenborgh**: data curation (equal), formal analysis (equal), writing – review and editing (equal). **Helena I. S. Nogueira**: data curation (equal), formal analysis (equal), writing – review and editing (supporting). **Scott G. Mitchell**: supervision (equal), writing – review and editing (supporting). **Ana Claro**: conceptualization (equal), methodology (equal), supervision (equal), writing – review and editing (supporting). **Teresa Ferreira**: conceptualization (lead), methodology (equal), supervision (lead), writing – original draft (lead), writing – review and editing (lead).

Acknowledgements

The authors would like to acknowledge Professor Fernanda Olival for her research, which unveiled the R_2 formulation and for sharing it, making a fundamental contribution to this work. The authors also thank G. Wanzeller Martins for the help with some colourimetric analysis and pH measurements in the mockups. Furthermore, the authors wish to acknowledge the professional support of the Interdisciplinary Thematic Platform from CSIC Open Heritage: Research and Society (PTI-PAIS). The authors are also very grateful for the support given by the research unit Fiber Materials and Environmental Technologies (FibEnTech-UBI), the Laboratorio de Microscopias Avanzadas (LMA) at Universidad de Zaragoza, the C^2TN at Instituto Superior Técnico (University of Lisbon), and the CICECO-Aveiro Institute of Materials, for offering access to their instruments and expertise. This work was conducted under the scope of the IRONIC (PTDC/ART-HIS/32327/2017) and Holy Bodies (10.54499/2022.01486.PTDC) projects. Funding was also provided through the strategic projects 10.54499/UID/PRR/04449/2025 (HERCULES Laboratory) and IN2Past 10.54499/LA/P/0132/2020. There was also the participation of UID/Multi/04349/2020, and the National Infrastructure Roadmap, LTHMFL-NECL, LISBOA-01-0145-FEDER-022096 and collaboration of the research unit Fiber Materials and Environmental Technologies (FibEnTech-UBI) on the extent of the project reference UIDB/00195/2020, funded by national funds through the IP/MCTES and CICECO-Aveiro Institute of Materials, UIDB/50011/2020, UIDP/50011/2020 & LA/P/0006/2020, financed by national funds through the FCT/MEC (PIDDAC).

Open access publication funding provided by FCT (b-on).

Funding

The work was supported by Fundação para a Ciência e a Tecnologia (Grants PTDC/ART-HIS/32327/2017, 10.54499/2022.01486.PTDC,

10.54499/UID/PRR/04449/2025, 10.54499/LA/P/0132/2020, UID/Multi/04349/2020, UIDB/00195/2020 and LA/P/0006/2020).

Conflicts of Interest

The authors declare no conflicts of interest.

Data Availability Statement

The data that support the findings of this study are available from the corresponding author upon reasonable request.

References

1. M. Aceto, A. Agostino, E. Boccaleri, and A. C. Garlanda, "The Vercelli Gospels Laid Open: An Investigation into the Inks Used To Write the Oldest Gospels in Latin," *X-Ray Spectrometry: An International Journal* 37 (2008): 286–292.

2. G. Nehring, O. Bonnerot, M. Gerhardt, M. Krutzsch, and I. Rabin, "Looking for the Missing Link in the Evolution of Black Inks," *Archaeological and Anthropological Science* 13 (2021): 142–148.

3. S. Kroustallis, "La escritura y sus materiales: pigmentos, tintas e instrumentos," in *El Soporte La Leng*, ed. P.S.M. la R. de Nájera, (2008), 133–166.

4. L. Raggetti, *Traces of Ink : Experiences of Philology and Replication*, ed. L. Raggetti (Brill, 2021).

5. V. Karpenko, and J. A. Norris, "Vitriol in the History of Chemistry," *Chemické Listy* 96 (2002): 997–1005.

6. S. Kroustallis, "Escribir en el siglo XVI: Recetas de la tinta negra española, *Torre los Lujanes Boletín la Real Soc*," *Económica Matr. Amigos del País* (2002): 99–112.

7. N. Teixeira, P. Nabais, V. de Freitas, J. A. Lopes, and M. J. Melo, "In-Depth Phenolic Characterization Of Iron Gall Inks By Deconstructing Representative Iberian Recipes," *Scientific Reports* 11 (2021): 1–11.

8. R. K. Feller and A. K. Cheetham, "Fe(III), Mn(II), Co(II), and Ni(II) 3,4,5-Trihydroxybenzoate (Gallate) Dihydrates; a New Family of Hybrid Framework Materials," *Solid State Science*, 8 (2006): 1121–1125.

9. A. Ponce, L. B. Brostoff, S. K. Gibbons, et al. "Elucidation of the Fe(III) Gallate Structure in Historical Iron Gall Ink," *Analytical Chemistry*, 88 (2016): 5152–5158.

10. C. H. Wunderlich, R. Weber and G. Bergerhoff, "Über Eisengallustinte," *ZAAC - Journal of Inorganic and General Chemistry*, 598 (1991): 371–376.

11. A. Lerf and F. E. Wagner, "Model Compounds of Iron Gall Inks – A Mössbauer Study," *Hyperfine Interactions*, 237 (2016): 13–18.

12. F. E. Wagner and A. Lerf, "Mössbauer Spectroscopic Investigation of Fe(II) and Fe(III) 3,4,5-Trihydroxybenzoates (Gallates) – Proposed Model Compounds for Iron-Gall Inks," *Journal of Inorganic and General Chemistry* 641, (2015): 2384–2391.

13. R. J. Díaz Hidalgo, R. Córdoba, P. Nabais, et al., "New Insights into Iron-Gall Inks through the Use of Historically Accurate Reconstructions," *Heritage Science* 6 (2018): 1–15.

14. V. Rouchon-Quillet, C. Remazeilles, J. Bernard, A. Wattiaux, and L. Fournes, "The Impact of Gallic Acid on Iron Gall Ink Corrosion," *Applied Physics A: Materials Science & Processing* 79 (2004): 389–392.

15. S. Zaccaron, *The Influence of Sizing and Iron-Gall Inks on the Kinetics and Degradation Mechanism of Cellulose in Sealed Vessel*, Ph.D. Thesis, (Universitá Ca'Foscari Venezia, 2014).

16. V. Rouchon and S. Bernard, "Mapping Iron Gall Ink Penetration within Paper Fibres Using Scanning Transmission X-ray Microscopy," *Journal of Analytical Atomic Spectrometry* 30 (2015): 635–641.

17. V. Rouchon, O. Belhadj, M. Duranton, A. Gimat, and P. Massiani, "Application of Arrehnius Law to DP and Zero-Span Tensile Strength Measurements Taken on Iron Gall Ink Impregnated Papers: Relevance of Artificial Ageing Protocols," *Applied Physics A: Materials Science & Processing* 122 (2016): 1–10.

18. A. Gimat, A. L. Dupont, H. Lauron-Pernot, S. Paris, V. Rouchon, and P. Massiani, "Behavior of Cellobiose in Iron-Containing Solutions: Towards a Better Understanding of the Dominant Mechanism of Degradation of Cellulosic Paper by Iron Gall Inks," *Cellulose* 24 (2017): 5101–5115.

19. V. Rouchon, M. Duranton, B. Cédric, E. Pellizzi, and B. Lavédrine, "Room-Temperature Study of Iron Gall Ink Impregnated Paper," *Analytical Chemistry* 83 (2011): 2589–2597.

20. J. Kolar, A. Štolfa, M. Strlič, et al., "Historical Iron Gall Ink Containing Documents - Properties Affecting their Condition," *Analytica Chimica Acta* 555 (2006): 167–174.

21. N. R. Perron, and J. L. Brumaghim, "A Review of the Antioxidant Mechanisms of Polyphenol Compounds Related to Iron binding," *Cell Biochemistry Biophysics* 53 (2009): 75–100.

22. C. Burgaud, V. Rouchon, A. Wattiaux, J. Bleton, R. Sabot, and P. Refait, "Determination of the Fe(II)/Fe(III) Ratio in Iron Gall Inks by Potentiometry: A Preliminary Study," *Journal of Electroanalytical Chemistry* 650 (2010): 16–23.

23. A. Gimat, A. Michelin, P. Massiani, and V. Rouchon, "Beneficial Effect of Gelatin on Iron Gall Ink Corrosio," *Heritage Science* 9 (2021): 1–13.

24. A. Barański, J. M. Łagan, T. Łojewski, *Ageing Stabilisation Pap*, Ed. M. Strlič, and J. Kolar, (2005).

25. Y. Liu, I. Kralj-cigić, and M. Strlič, "Kinetics of Accelareted Degradation of Historical Iron Gall-Containing Paper," *Polymer Degradatoion and Stability* (2017): 1–19.

26. J. Neevel, 8th Congr. The Development of a New Conservation Treatment for Ink Corrosion, in Based on the Natural Anti-oxidant Phytate, *IADA*, eds.: K. Mogens, and J. Palm, (IADA Preprints, 1995), 93–100.

27. D. La Camera, "Crystal Formations within Iron Gall Ink: Observations And Analysis," *Journal of the American Institute for Conservation* 46 (2007): 153–174.

28. S. Zervos, and A. Moropoulou, "Cotton Cellulose Ageing in Sealed Vessels. Kinetic model of Autocatalytic Depolymerization, *Cellulose* 12 (2005): 485–496.

29. A. Ferretti, F. Sabatini, and I. Degano, "A Model Iron Gall Ink: An In-Depth Study of Ageing Processes Involving Gallic Acid," *Molecules* 27 (2022): 1–17.

30. ISO 5630-3, 1996; *Paper and Board — Accelerated Ageing — Part 3: Moist Heat Treatment at 80 Degrees C and 65% Relative Humidity*, (International Organization for Standardization, 1996).

31. SIST EN 15886:2010: "Conservation of Cultural Property - Test Methods - Colour Measurement of Surfaces," (2010).

32. M. F. Lü, E. V. Tsipis, J. C. Waerenborgh, et al., *Journal of Power Sources* 206 (2012): 59–69.

33. UNE 57039-1 *Pulps. Cellulose in Dilute Solutions. Determination of Limiting Viscosity Number. Part 1: Method in Cupri-Ethylene-Diamine (CED) Solution*, (1992).

34. L. Segal, J. J. Creely, A. E. Martin, and C. M. Conrad, "An Empirical Method for Estimating the Degree of Crystallinity of Native Cellulose Using the X-ray Diffractometer," *Textile Research Journal* 29 (1959): 786–794.

35. A. D. French, and M. Santiago Cintrón, "Cellulose Polymorphy, Crystallite Size, and the Segal Crystallinity Index," *Cellulose* 20 (2013): 583–588.

36. M. Poletto, A. J. Zattera, M. M. C. Forte, and R. M. C. Santana, "Thermal decomposition of wood: Influence of Wood Components and Cellulose Crystallite Size," *Bioresource Technology* 109 (2012): 148–153.

37. ISO 536 2019, *Paper and Board — Determination of Grammage*, (International Organization for Standardization, 2019).

38. ISO 534 2011, *Paper and Board — Determination of Thickness, Density and Specific Volume*, (International Organization for Standardization, 2011).

39. ISO 5636-5 2014, *Paper and Board — Determination of Air Permeance (Medium Range) — Part 5: Gurley Method*, (International Organization for Standardization, 2014).

40. ISO 15361 2000, *Pulps — Determination of Zero-Span Tensile Strength, Wet or Dry*, (International Organization for Standardization, 2000).

41. ISO 1924-2 2008, *Paper and Board — Determination of Tensile Properties — Part 2: Constant Rate of Elongation Method (20 Mm/Min)*, (International Organization for Standardization, 2008).

42. ISO 2758 2014, *Paper — Determination of Bursting Strength*, (International Organization for Standardization, 2014).

43. M. C. Sistach, and I. Espadaler, "Organic and Inorganic Components of Iron Gall inks," in *ICOM Committee for Conservation* (Barcelona, 1993): 485–490.

44. V. Corregidor, R. Viegas, L. M. Ferreira, and L. C. Alves, "Study of Iron Gall Inks, Ingredients and Paper Composition Using Non-Destructive Techniques," *Heritage*, 2 (2019): 2691–2703.

45. L. Falcão, and M. E. M. Araújo, "Tannins Characterization in Historic Leathers by Complementary Analytical Techniques ATR-FTIR, UV-Vis and Chemical Tests," *Journal of Culturnal Heritage* 14 (2013): 499–508.

46. A. A. Kaminari, S. C. Boyatzis, and A. Alexopoulou, "Linking Infrared Spectra of Laboratory Iron Gall Inks Based on Traditional Recipes with their Material Components," *Applied Spectroscopy* 72 (2018): 1511–1527.

47. A. Espina, M. V. Cañamares, Z. Jurašeková, and S. Sanchez-Cortes, "Analysis of Iron Complexes of Tannic Acid and other Related Polyphenols as Revealed by Spectroscopic Techniques: Implications in the Identification and Characterization of Iron Gall Inks in Historical Manuscript," *ACS Omega* 7 (2022): 27937–27949.

48. J. Guo, Y. Ping, H. Ejima, et al., "Engineering Multifunctional Capsules Through the Assembly of Metal-Phenolic Networks," *Angewandtle Chemie International Edition* 53 (2014): 5546–5551.

49. M. Bicchieri, M. Monti, G. Piantanida, F. Pinzari, and A. Sodo, "Non-Destructive Spectroscopic Characterization of Parchment Documents," *Vibrational Spectroscopy* 55 (2011): 267–272.

50. B. C. Smith, (2018), "Spectroscopy, Carbonyl Group, Part V Carboxylates—Coming Clean," accessed January 19 (2025): 20–23, https://www.spectroscopyonline.com/.

51. G. B. Deacon, R. J. Phillips, "Relationship between the Carbon-Oxigen Stretching Frequencies of Carboxylato Complexes and the Type of Carboxylate Coordination," *Coordination Chemistry Reviews* 33 (1980): 227–250.

52. M. A. Rahim, K. Kempe, M. Müllner, et al., "Surface-Confined Amorphous Films From Metal-Coordinated Simple Phenolic Ligands," *Chemistry of Materials* 27 (2015): 5825–5832.

53. S. N. Reddy, P. S. Rao, R. V. S. S. N. Ravikumar, B. J. Reddy, and Y. P. Reddy, "Spectral Investigations on Melanterite Mineral from France," *Spectrochimica Acta - Part A: Molecular and Biomolecular Spectroscopy* 57 (2001): 1283–1287.

54. M. Lacalamita, G. Ventruti, G. Della Ventura, F. Radica, D. Mauro, and E. Schingaro, "In situ High-Temperature X-Ray Powder Diffraction and Infrared Spectroscopic Study of Melanterite, FeSO4·7H2O," *Minerals* 11 (2021): 11.

55. C. Remazeilles, V. Rouchon-Quillet, and J. Bernard, "Influence of Gum Arabic on Iron-Gall Ink Corrosion Part II: Observation and Elemental Analysis of Originals," *Restaurator* 26 (2005): 118–133.

56. A. S. Lee, P. J. Mahon, and D. C. Creagh, Raman Analysis of Iron Gall Inks on Parchment," *Vibrational Spectroscopy* 41 (2006): 170–175.

57. J. Torres, S. Domínguez, M. F. Cerdá, et al.,, "Solution Behaviour of Myo-Inositol Hexakisphosphate in the Presence of Multivalent Cations. Prediction of a Neutral Pentamagnesium Species under Cytosolic/ Nuclear Conditions," *Journal of Inorganic Biochemistry* 99 (2005): 828–840.

58. A. Lee, and C. Whitley, D. Creagh, "Study on the light Fading of Iron Gall Inks on Parchment," in *AICCM Symp*, (2006), 55–68.

59. C. Burgaud, V. Rouchon, P. Refait, and A. Wattiaux, "Mössbauer Spectrometry Applied to the Study of Laboratory Samples Made of Iron Gall Ink," *Applied Physics A Materials Science and Processing* 92 (2008): 257–262.

60. Hudson Institute of Mineralogy, Mindata, Melanterite. (2021), https://doi.org/10.1180/mgm.2021.43.

61. E. Ehlers, and D. Stiles, "Melanterite-Rozenite Equilibrium," *Mineral notes* 50 (1965): 1457–1461.

62. A. G. Mitchell, "The Preparation and Characterization of Ferrous Sulphate Hydrates," *Journal of Pharmacy and Pharmacology* 36 (1984): 506–510.

63. M. D. Dyar, E. Breves, E. Jawin, et al., "What lurks in the Martian rocks and soil? Investigations of Sulfates, Phosphates, and Perchlorates: Mössbauer Parameters of Iron in Sulfate Minerals," *American Mineralogist* 98 (2013): 1943–1965.

64. J. Gust, and J. Suwalski, "Use of Mössbauer Spectroscopy to Study Reaction Products of Polyphenols and Iron Compounds, Corrosion," *Corrosion* 50 (1994): 355–365.

65. M. Ciglanská, V. Jančovičová, B. Havlínová, Z. Machatová, and V. Brezová, "The Influence of Pollutants on Accelerated Ageing of Parchment with Iron Gall Inks," *Journal of Cultural Heritage* 15 (2014): 373–381.

66. K. Dzinavatonga, K. Bharuth-Ram, and T. R. Medupe, "Mössbauer Spectroscopy Analysis of Valence State of Iron in Historical Documents Obtained from the National Library of South Africa," *Journal of Cultural Heritage* 16 (2015): 377–380.

67. A. Lerf, F. E. Wagner, M. Dreher, T. Espejo, J. L. Pérez-Rodríguez, "Mössbauer Study of Iron Gall Inks on Historical Documents," *Heritage Science* 9 (2021): 1–14.

68. B. Wagner, E. Bulska, B. Stahl, and M. Heck, H. M. Ortner, "Analysis of Fe Valence States in Iron-Gall Inks from XVIth Century Manuscripts by 57Fe Mössbauer Spectroscopy," *Analytica Chimica Acta* 527 (2004): 195–202.

69. J. G. Neevel, "Phytate: A Potential Conservation Agent for the Treatment of Ink Corrosion Caused by Iron Gall Inks," *Restaurator* 16 (1995): 143–160.

70. G. Pliego, J. A. Zazo, J. A. Casas, and J. J. Rodriguez, "Fate of Iron Oxalates in Aqueous Solution: The Role of Temperature, Iron Species and Dissolved Oxygen," *Journal of Environmental Chemical Engineering* 2 (2014): 2236–2241.

71. K. Lee, and M. Inaba, "Moist Heat Accelerated Aging Test of Naturally Aged Paper by Suspension Method," *Restaurator* 34 (2013): 81–100.

72. H. Bansa, "Accelerated ageing of paper: Some Ideas on its Practical Benefit," *Restaurator* 23 (2002): 106–117.

73. B. Zhang, J. Cai, C. Q. Duan, M. J. Reeves, and F. He, "A Review of Polyphenolics in Oak Woods," *International Journal of Molecular Sciences* 16 (2015): 6978–7014.

74. N. Ferrer, and M. Sistach, "Analysis of Sediments on Iron Gall Inks in Manuscripts," *Restaurator* 34 (2013): 175–193.

75. M. Nunes, C. Relvas, F. Figueira, et al., "Analytical and Microbiological Characterization of Paper Samples Exhibiting Foxing Stains," *Microscopy and Microanalysis* 21 (2015): 63–77.

76. F. Carrillo, X. Colom, J. J. Suñol, and J. Saurina, "Structural FTIR Analysis and Thermal Characterisation of Lyocell and Viscose-Type Fibres," *Europen Polymer Journal* 40 (2004): 2229–2234.

77. D. Ciolacu, F. Ciolacu, and V. Popa, "Amorphous Cellulose - Structure and Characterisation," *Cellulose Chemistry and Technology* 25 (2011): 13–21.

78. T. Łojewski, P. Miśkowiec, M. Molenda, A. Lubańska, and J. Łojewska, "Artificial Versus Natural Ageing of Paper. Water Role in Degradation Mechanisms," *Applied Physics A: Materials Science and Processing* 100 (2010): 625–633.

79. S. Cichosz, and A. Masek, "Ir Study on Cellulose with the Varied Moisture Contents: Insight into the Supramolecular Structur," *Materials* 13 (2020): 1–22.

80. J. Łojewska, P. Miśkowiec, T. Łojewski, and L. M. Proniewicz, "Cellulose Oxidative and Hydrolytic Degradation: In Situ FTIR approach," *Polymer Degradation and Stability* 88 (2005): 512–520.

81. U. Henniges, R. Reibke, G. Banik, et al., "Iron Gall ink-Induced Corrosion of Cellulose: Aging, Degradation and Stabilization. Part 2: Application on Historic Sample Material," *Cellulose* 15 (2008): 861–870.

82. L. Csefalvayová, B. Havlínová, M. Čeppan, and Z. Jakubíková, "The Influence of Iron Gall Ink on Paper Ageing," *Restaurator* 28 (2007): 129–139.

83. M. Ursescu, T. Măluţan, and S. Ciovică, Iron Gall inks Influence on Papers' Thermal Degradation FTIR Spectroscopy Applications," *European Journal of Science and Theology* 5 (2009): 71–84.

84. T. Tribulová, F. Kačík, D. V. Evtuguin, I. Čabalová, and J. Ďurkovič, "The Effects Of Transition Metal Sulfates On Cellulose Crystallinity During Accelerated Ageing Of Silver Fir Wood," *Cellulose* 26 (2019): 2625–2638.

85. A. L. Dupont, and G. Mortha, "Comparative Evaluation of Size-Exclusion Chromatography and Viscometry for the Characterisation of Cellulose," *Journal of Chromatography A* 1026 (2004): 129–141.

86. T. Łojewski, K. Zieba, and J. Łojewska, "Size exclusion chromatography and viscometry in paper degradation studies. New Mark-Houwink Coefficients for Cellulose in Cupri-Ethylenediamine," *Journal of Chromatography A* 1217 (2010): 6462–6468.

87. R. Evans, and A. F. A. Wallis, "Cellulose Molecular Weights Determined by Viscometry," *Journal of Applied Polymer Science* 37 (1989): 2331–2340.

88. A. Van Heiningen, M. S. Tunc, Y. Gao, and D. Da Silva Perez, "Relationship between Alkaline Pulp Yield and the Mass Fraction and Degree of Polymerization of Cellulose in The Pulp," *Journal of Pulp and Paper Science* 30 (2004): 211–217.

89. S. Park, J. Baker, M. Himmel, P. Parilla, and D. Johnson, "Cellulose Crystallinity Index: Measurement Techniques And Their Impact on Interpreting Cellulase Performance," *Biotechnology Biofuels Bioproduct* 3 (2010): 10.

90. A. French, "Cellulose" in Encyclopedia of Biophysics, ed. G. Roberts, and A. Watts (Springer, 2018), 1–9.

91. S. Nam, A. D. French, B. D. Condon, and M. Concha, "Segal Crystallinity index Revisited by the Simulation of X-Ray Diffraction Patterns of Cotton Cellulose Iβ and Cellulose II," *Carbohydratre Polymer* 135 (2016): 1–9.

92. U. P. Agarwal, S. A. Ralph, C. Baez, R. S. Reiner, and S. P. Verrill, "Effect of sample moisture content on XRD-Estimated Cellulose Crystallinity Index and Crystallite Siz," *Cellulose* 24 (2017): 1971–1984.

93. M. T. R. Bhuiyan, N. Hirai, N. Sobue, "Changes of Crystallinity in Wood Cellulose by Heat Treatment Under Dried and Moist Conditions," *Journal Wood Science* 46 (2000): 431–436.

94. M. Cocca, L. D'Arienzo, and L. D'Orazio, "Effects of Different Artificial Agings on Structure and Properties of Whatman Paper Samples," *International Scholarly Research Notices* 2011 (2011): 1–7.

95. Y. W. Chen, H. V. Lee, and S. B. Abd Hamid, "Preparation and Characterization Of Cellulose Crystallites via Fe(III)-, Co(II)- and Ni(II)-Assisted Dilute Sulfuric Acid Catalyzed Hydrolysis Process," *Journal of Nano Research* 41 (2016): 96–109.

96. T. Inagaki, H. W. Siesler, K. Mitsui, and S. Tsuchikawa, "Difference of the Crystal Structure of Cellulose in Wood After Hydrothermal and Aging Degradation: A NIR Spectroscopy and XRD Study," *Biomacromolecules* 11 (2010): 2300–2305.

97. U. J. Kim, S. H. Eom, M. Wada, "Thermal decomposition of native cellulose: Influence on crystallite size," *Polymer Degradation Stability* 95 (2010): 778–781.

98. C. Driemeier, M. T. B. Pimenta, G. J. M. Rocha, et al., "Evolution of Cellulose Crystals During Prehydrolysis and Soda Delignification of Sugarcane Lignocellulose," *Cellulose* 18 (2011): 1509–1519.

99. B. R. Manjunath, N. Peacock, "Recrystallization of the cellulose I Lattice in Mercerized and Regenerated Cellulose Fibers," *Textile Research Journal* 39 (1969): 70–77.

100. J. Gassan, A. K. Bledzki, "Possibilities for Improving the Mechanical Properties of Jute/Epoxy Composites by Alkali Treatment of Fibre," *Composites Science Technology* 59 (1999): 1303–1309.

101. S. Zervos, "Natural and accelerated ageing of cellulose and paper: A literature review," in Cellulose: Structure and Properties, Derivatives and Industrial Uses, (2010) 115–203.

102. L. Taylor, J. Phipps, S. Blackburn, R. Greenwood, D. Skuse, "Using Fibre Property Measurements to Predict the Tensile Index of Microfibrillated Cellulose Nanopaper," *Cellulose* 27 (2020): 6149–6162.

103. M. Feber, J. Havermans, P. Defize, "Iron-Gall Ink Corrosion: A Compound-Effect Study," *Restaurator* 21 (2000): 204–212.

Supporting Information

Additional supporting information can be found online in the Supporting Information section. **Supporting Fig. S1:** ATR-FT-IR spectra of the dried gallnut extracts used to produce the R_1 (two-day period) and R_2 inks (nine-day period) and commercial gallic and tannic acids. Assignments for the labelled bands in the dried gallnut extract spectrum are presented in Table SI.3. The spectra are normalised and vertically offset for clarity. **Supporting Fig. S2:** Raman spectra of the R_1 and R_2 ppts showing the region of interest (2000-400 cm^{-1}). The spectra are vertically offset for clarity. **Supporting Fig. S3:** X-ray diffraction patterns recorded for the dried inks (top) and the precipitates (bottom). g – gypsum ($CaSO_4 \cdot 2H_2O$); m – melanterite ($FeSO_4 \cdot 7H_2O$); r - rozenite ($FeSO_4 \cdot 4H_2O$); s – szomolnokite ($FeSO_4 \cdot H_2O$). The spectra are vertically offset for clarity, and colour grading is used for better visualisation. **Supporting Fig. S4:** Mössbauer spectra of $R_1\_d_1$ (a), $R_1\_d_2$ (b), $R_2\_d_1$ (c) and $R_2\_d_2$ (d) taken at 295 K. The lines over the experimental points (green) on the spectra are the sum of the doublets, which are slightly shifted for clarity. The red line represents a Fe(III) species, and the light blue line indicates a Fe(II) species constituted by melanterite or rozenite or mixtures of both (Table SI.7). The percentage bar is an indication of the absorption intensity as a fraction of the baseline transmission. **Supporting Fig. S5:** Mössbauer spectra of $R_1\_d_1$ (a) and $R_1\_d_2$ (b) (right), and $R_2\_d_1$ (c) and $R_2\_d_2$ (d) (left) taken at 80 K. The lines over the experimental points (green) in the spectra are the sum of the doublets, which are slightly shifted for clarity. The red line indicates a Fe(III) species, the blue line represents Fe(II) in szomolnokite, and the light blue line corresponds to a Fe(II) species constituted by melanterite or rozenite or mixtures of both (Table SI.7). The percentage bar is an indication of the absorption intensity as a fraction of the baseline transmission. **Supporting Fig. S6:** Mössbauer spectra of $R_1\_ppt_1$ (a), $R_1\_ppt_2$ (b), $R_2\_ppt_1$ (c) and $R_2\_ppt_2$ (d) taken at 295 K. The lines over the experimental points (green) on the spectra are the sum of the doublets, which are slightly shifted for clarity. The red line represents a Fe(III) species, and the light blue line corresponds to a Fe(II) species constituted by melanterite or rozenite or mixtures of both (Table SI.7). The percentage bar is an indication of the absorption intensity as a fraction of the baseline transmission. **Supporting Fig. S7:** Mössbauer spectra of $R_1\_ppt_1$ (a), $R_1\_ppt_2$ (b), $R_2\_ppt_1$ (c) and $R_2\_ppt_2$ (d) taken at 80 K. The lines over the experimental points (green) on the spectra are the sum of the doublets, which are slightly shifted for clarity. The red line represents a Fe(III) species, and the light blue line represents a Fe(II) species constituted by melanterite or rozenite or mixtures of both (Table SI.7). The percentage bar is an

indication of the absorption intensity as a fraction of the baseline transmission. **Supporting Fig. S8:** a) colour variation (ΔE^*_{ab}) between the reference samples (S), R1 and R2 mockups at each ageing period (t_1-t_4) and their corresponding unaged counterparts; b) ΔL^*, Δa^*, Δb^* coordinates; c) pH values. Colour grading is used for better visualisation. **Supporting Fig. S9:** Mössbauer spectra of $R_1b\_t_0$ (a), $R_1b\_t_1$ (b) and $R_1b\_t_2$ (c) taken at 295 K. The lines over the experimental points (green) on the spectra are the sum of the doublets, which are shown slightly shifted for clarity. The red line represents a Fe(III) species, and the sky blue line represents an oxalate Fe(II) species (see Table SI.11). The percentage bar is an indication of the absorption intensity as a fraction of the baseline transmission. **Supporting Fig. S10:** Mössbauer spectra of $R_2b\_t_0$ (a), $R_2b\_t_1$ (b) and $R_2b\_t_2$ (c) taken at 295 K (left) and 80 K (right). The lines over the experimental points (green) on the spectra are the sum of the doublets, which are shown slightly shifted for clarity. The red line represents a Fe(III) species, the sky blue line represents an oxalate Fe(II) species, and the blue line represents szomolnokite (see Table SI.11). The percentage bar is an indication of the absorption intensity as a fraction of the baseline transmission. **Supporting Fig. S11:** ATR-FT-IR full region spectra of the unaged (t_0) and aged (t_1-t_4) reference sample (S), with insets focusing on the region of interest (1800-700 cm^{-1}) and highlighting major spectral differences associated with the structural changes in the cellulose support. Key bands discussed in the main body text were labelled. The spectra are normalised and vertically offset for clarity, and colour grading is used for better visualisation. **Supporting Fig. S12:** Average DP and std values (σ) for the unaged (t_0) and aged (t_1, t_2) S samples, along with the R1 and R2 mockups (left), and the percentage decrease in DP values (right). **Supporting Fig. S13:** XRD patterns of the unaged (t_0) and aged (t_1-t_4): a) reference sample (S); b) R_1 mockups; c) R_2 mockups. The Miller indices for the main peaks ascribed to cellulose Iβ are indicated in the diffractograms. The spectra are vertically offset for clarity, and colour grading is used to enhance visualisation. **Supporting Fig. S14:** Young's modulus values for the unaged (t_0) and aged (t_1, t_2) S samples and mockups. Colour grading is used for better visualisation. **Supporting Table. S1:**Conversion of the ancient units in the historical recipes into the units in the International System of Units, with millilitre (mL) as a particular name for the cubic centimetre (cm^3). **Supporting Table S3:** Wavenumber (cm^{-1}) and tentative assignment of the absorption bands in ATR-FT-IR spectra of the starting materials: dried nine day gallnut extract[a] and iron sulfate. **Supporting Table S4:** Wavenumber (cm^{-1}), tentative assignment, and interpretation of the absorption bands in ATR-FT-IR spectra of fresh ($R_1\_d_1$, $R_2\_d_1$) and aged ($R_1\_d_2$, $R_2\_d_2$) dried inks. **Supporting Table S5:** Wavenumber (cm^{-1}), tentative assignment, and interpretation of the absorption bands in ATR-FT-IR spectra of fresh ($R_1\_ppt_1$, $R_2\_ppt_1$) and aged precipitates ($R_1\_ppt_2$, $R_2\_ppt_2$). **Supporting Table S6:** Raman shift (cm^{-1}), tentative assignment, and interpretation of the Raman bands in spectra of samples $R_1\_ppt_1$, $R_1\_ppt_2$, $R_2\_ppt_1$, $R_2\_ppt_2$. **Supporting Table S7:** Parameters estimated from the Mössbauer spectra taken at 295 and 80 K of the dried inks and precipitates. **Supporting Table S8:** Photographic images of the unaged and aged mockups. **Supporting Table S9:** ΔL^*, Δa^*, Δb^*, $\Delta E^*_{ab}$$, and std (σ) values for the reference sample (S) and the R_1 and R_2 mockups. To ensure reproducibility, three measurements were taken of both the unaged and aged S samples, as well as in the inked areas of the unaged and aged mockups. The average of these three measurements is presented. **Supporting Table S10:** pH and std (σ) values for the unaged (t_0) and aged (t_1-t_4) reference (S) sample and the R_1b and R_2b mockups. **Supporting Table S11:** Parameters estimated for the mockups from the Mössbauer spectra taken at 295 and 80 K. **Supporting Table S12:** Average DP and std values (σ) for the unaged (t_0) and aged (t_1, t_2) S samples, along with the R_1 and R_2 mockups (left), and the percentage decrease in DP values (right).